Coupled Length Scales in Eroding Landscapes

by

Kelvin Ka Wing Chan

Submitted to the Department of Earth, Atmospheric, and Planetary Sciences
in partial fulfillment of the requirements for the degree of

Master of Science in Earth and Planetary Sciences

at the

MASSACHUSETTS INSTITUTE OF TECHNOLOGY

May 1999
[June 1999]

Author ....
Department of Earth, Atmospheric, and Planetary Sciences
May 7, 1999

Certified by ....
Daniel H. Rothman
Professor
Thesis Supervisor

Accepted by ....
Ronald G. Prinn
Department Head, Department of Earth, Atmospheric, and Planetary Sciences

Coupled Length Scales in Eroding Landscapes

by

Kelvin Ka Wing Chan

Submitted to the Department of Earth, Atmospheric, and Planetary Sciences
on May 7, 1999, in partial fulfillment of the
requirements for the degree of
Master of Science in Earth and Planetary Sciences

Abstract

We propose a method to study natural topography by means of local transform. A nonlinear local transform $\mathcal{A}_{\ell_c}[h(\mathbf{x})]$ of the elevation field $h(\mathbf{x})$ is used to determine a *director* field of anisotropy $\mathbf{a}(\mathbf{x})$. The *director* field is directly related to local small-scale channel-like features. From study of the correlations of these with large-scale structure of drainage basins, characteristic coupling length scales are found which indicate an important breaking of scale invariance. We also show that these length scales are related to the average sizes of the individual drainage basins. Our study demonstrates one way in which landscape patterns of unknown origin may be quantitatively analyzed to determine the kind of mechanisms that have eroded them.

Thesis Supervisor: Daniel H. Rothman
Title: Professor

Acknowledgments

Zeroth, my thanks go to our Almighty Boss above, who kindly created us and this universe (which is so complicated and interesting that we shall never be bored). Without Him, nothing ever is possible.

First, I thanked my parents, Kai Ping and Wai Chi Chan. They obviously had spent many hours of their lives to make sure that I am doing ok and lead a balanced life style (which I find it very difficult to achieve at MIT). They have supported me both financially and psychologically to get through my undergraduate years and now my graduate years. I also thanked my brother, Kelly Chan, for his kind and timely reminder of the sanitary condition of our bathroom and kitchen.

At MIT, my warmest thanks go to my advisor Dan Rothman, who introduced and initiated me into the world of complex and nonlinear dynamical systems. Without his many hours of advising and humorous remarks, this thesis will never be possible. I also thanked my co-advisor John Grotzinger, who had provided me the opportunity and funding to work on an interesting geological problem with some astrobiological relevance. He also invited me to join his geological field trips in NWT Canada (summer 1996) and New Mexico (spring 1999), the two most unique and thrilling academic experience I ever had and unlikely to be duplicated elsewhere. I also thanked Yen Feder and Andrea Rinaldo for their helpful discussions and for giving me important insights into my research.

I was also fortunate to have support and companies from friends: Ernie Yeh, Albert To, Edwin Cheung, Connie Cheng, Edward Wong, Oliver Yip, Agnes Wang, Jimmy Wong, KM Lau, Philip Lo, Oliver Yip, Agnes Wang, Jimmy Wong, KM Lau, James Mak, Wing Wah and Dorcas Sung, Zachary Lee, (please forgive me if I forgot to mention names which you think I should) and many other brothers and sisters at the Hong Kong Student Bible Study and Daniel Fellowship, whom I had shared my stresses and joys with. Millions of thanks go to you all.

Last but not least, my gratitude extends to my colleagues and friends at EAPS: Peter Dodds, Romu Pastor-Satorras, Olav van Genabeek, and Wesley Watters who

had all helped enormously in my research and course works. I also thank Joshua Weitz and Davide Stelitano, who sometimes kept me company late at night at Bldg 54.

Contents

List of Figures

List of Tables

Chapter 1

Introduction

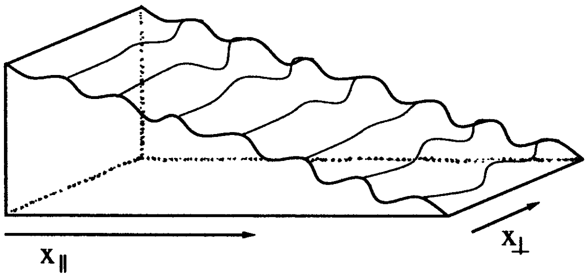

Figure 1-1: An inclined plane possesses two directions. $x_{||}$ (tip) is in the direction of dominant flow and $x_{\perp}$ (strike) is the direction perpendicular to this.

Natural landscapes can be influenced by multitude of factors that may be physical, chemical, or biological in origins. Geomorphology principally concerns itself with the study of surface features and structures influenced by *exogenic* processes (those originated from outside the solid earth) [2]. These included fluvial erosion, glacial and periglacial erosion, avalanches, aquatic effects, aeolian erosion (wind and sand movement), biological activities (vegetation), etc. But in general, at relatively large scales, geomorphology is dominated by tectonic motion (*endogenic processes*) while at shorter scales, surficial erosion plays an important role.

Despite the diversity of processes and highly heterogenuous geological conditions (in time and space), landscapes generally erode in part due to material transport [2] and the resultant shearing stresses imposed by the flow. However, the exact formulation of a theory for fluvial erosion is not known. It is well known that natural landscapes possess fractal (or self-affine) geometry [1, 3, 4] and geomophological complexity can be observed over many length scales. The underlying theory must therefore account for all these observations at the appropriate scales. This concept of self-affinity of natural landscapes has provoked the suggestion that erosion follows mechanisms similar to a wide variety of surface growth problems [5].

More recent studies of fractal nature and minimization principle of river basins and networks had involved concepts and ideas known as optimal channel networks and self-organized criticality [7, 8]. This indicates that careful study of macroscopic patterns can yield fundamental insights into the microscopic basic mechanisms [11]. Therefore, a more detailed and physically motivated quantitative study of topography may be needed to yield information about features unique to fluvial erosion.

It may be true that models of fluvial erosion involve some common general considerations such as symmetries, range of interactions, nonlinearity, conservation laws, etc., which do not all depend on system details and give rise to universal features in pattern formation [11]. But quantitative features special to eroded landscapes must be studied if one wants to gain access to the detailed dynamics of landscape evolution.

Recent observation and theoretical works [6] show that statistical properties of landscape can be influenced by the dominant direction of flow on its surface. Specifically, they compute the height-height correlation function $C(\mathbf{r}) = \langle |h(\mathbf{x}+\mathbf{r}) - h(\mathbf{x})|^2 \rangle_{\mathbf{x}}^{1/2}$. The most ubiquitous and consistent observation is that $C(x_\perp) > C(x_\parallel)$ where $x_\parallel$ is in the direction of the flow (dip) and $x_\perp$ is orthogonal (strike) to it. See Fig. 1-1. For self-affine surfaces, $C(x) \sim x^\alpha$. Physically, this corresponds to the observation that topography is rougher transverse to the flow than in the direction parallel to the flow. A nonlinear model was proposed resulting in a stochastic PDE of growth which predicts different roughness exponents $\alpha_\parallel$ and $\alpha_\perp$ for the two directions. This has been observed in a submarine canyon off the coast of Oregon [6]. For real landscapes in general (rather than an incline with an obvious downflow direction), the directions of main flow will depend on the topographic structure observed at different scales. Furthermore, the self-affinity and/or geometric complexity of natural landscapes imply that the local statistical anisotropy be also scale-dependent.

Inspired by these simple observations and motivated by the need of a quantitative study of eroded topography, we raise some important questions concerning natural landscapes: How does local anisotropic structure (related to local channelization) correlates with the general topographic features (related to relief structures of drainage basins)? At what length scales? Are there optimum scales at which they become most strongly correlated? If such scales do exist, what are their physical interpretations and how do they relate to the physical topography? Conceptually, the two aspects (anisotropy and topographic structure) involved are coupled via fluvial erosion and the preferred directions of material transport along the surface. This indicates that the questions we posed are relevant investigations of the general characters of fluvial erosion of natural landscapes. On the other hand, the nonlinear nature of surficial growth is likely to be a consequence of the interactions of processes operating at different length (or time) scales. These couplings of length scales may manifest themselves in the correlation between large and small scale features of the topography.

This prompts us to study empirically the correlation between surficial anisotropy (local channels) and topographic structures (drainage basins). We propose a way of studying this surficial anisotropic structure using local transforms and correlation functions. The method involved is largely inspired by works on the analysis of pattern-forming systems [9, 10]. In the following chapters, we first introduce the method we use and some assumptions we make. We then present results from the study of topography which ranges from the western flank of the Sierra Nevada mountains to the eastern edge of the Central Valley. This leads to the discussion of how our findings connect with some important results in geomorphology concerning erosion, total contributing area, and local slope. Finally, we discuss the various physical implications and interpretations of the empirical results have on some general characteristics of fluvial erosion.

Chapter 2

The method

2.1 Apparent dip direction and anisotropy in fluvial erosion

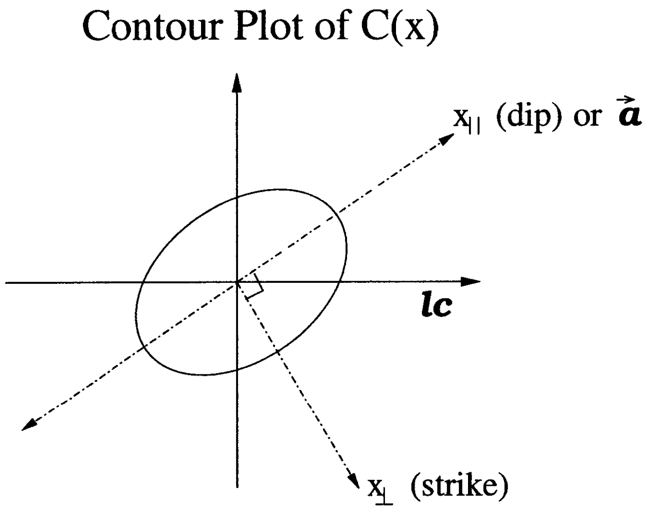

Figure 2-1: Contour plot of $C(\mathbf{x})$ assuming validity of linear theory and $x \ll L$ where L is the system size

Since a preferred direction of flow leaves a statistical signature in the height-height correlation function $C(\mathbf{x}) = \langle |h(\mathbf{x}'+\mathbf{x}) - h(\mathbf{x}')|^2\rangle_{\mathbf{x}'}^{1/2}$. It is in principle possible to infer the original direction of dominant flow by studying the structure of $C(\mathbf{x})$ alone. In the linear theory and the limit $x \ll L$ where L is the system size, one expects elliptic contours for $C(\mathbf{x})$, as depicted in Fig. 2-1. To demonstrate this, we plot the contours of $C(\mathbf{x})$ for a fracture surface (after López and Schmittbuhl) and a synthetic isotropic self-affine surface of fractal dimension 1.2 in Fig. 2-2. Note that at small $\mathbf{x}$, the contour is elliptical for the fracture surface (which is known to be anisotropic) but circular for the isotropic surface.

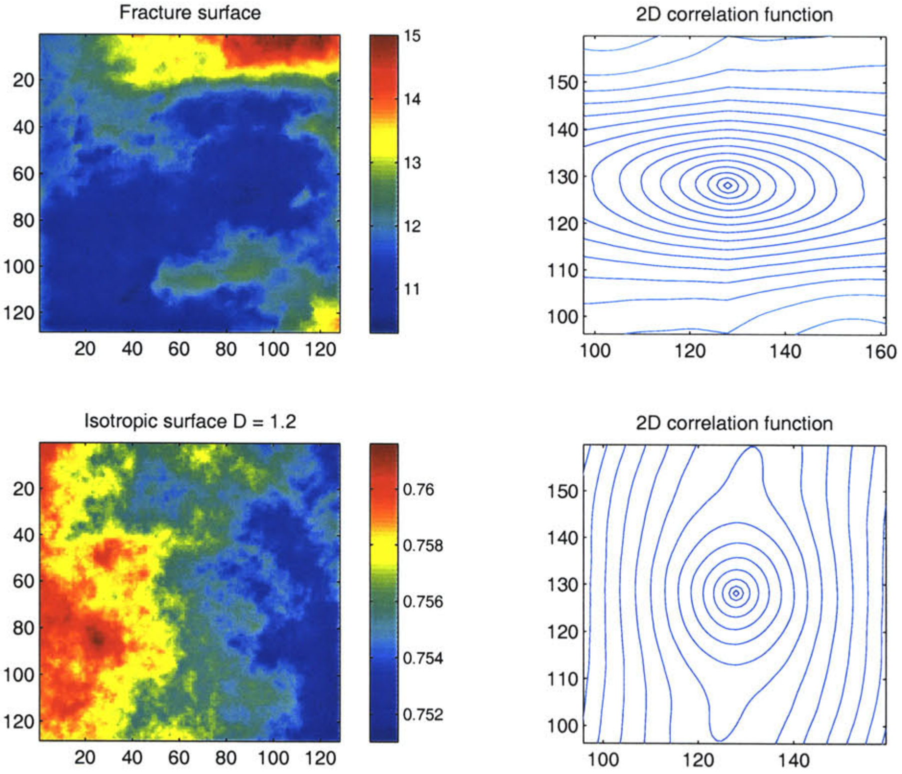

Figure 2-2: Contours of $C(\mathbf{x})$ for a fracture surface and a synthetic isotropic self-affine surface of $D \sim 1.2$. Note that at small $\mathbf{x}$ (near the center), the contour is elliptical for the fracture surface (which is known to be anisotropic) but circular for the isotropic surface.

When applied to natural topography, from the semi-major and semi-minor axes of the ellipse, one can deduce an *apparent* dip direction. This can also be regarded as the local anisotropic director field $\mathbf{a}(\mathbf{x})$. A director is a vector with angular orientation but no direction: $\mathbf{a}$ is indistinguishable from $-\mathbf{a}$. One may represent it by a straight line, but no arrow to indicate the direction. This is the conceptual justification of an *apparent* dip direction. But we shall deduce this through another method. This is largely inspired by recent applications of wavelet transforms in the analysis of pattern formation [9].

2.2 Wave packet and local transformations

We first define the kernel or the analyzing function of our local transform (with a wavenumber $|\mathbf{k}|$):

$$W_{\ell_c}(\mathbf{x},\phi) = \frac{1}{\ell_c^2}\, e^{i\mathbf{k}_\phi\cdot\mathbf{x}}\, g\!\left(\frac{\mathbf{x}}{\ell_c}\right), \tag{2.1}$$

where

$$\begin{aligned} \mathbf{k}_\phi &= \frac{2\pi}{\lambda}(\cos\phi,\sin\phi),\ \ 0 \le \phi < 2\pi \\ g(\mathbf{y}) &= \exp\left(-8y^2\right). \end{aligned} \tag{2.2}$$

This is equivalent to a plane wave with an amplitude modulated by a Gaussian envelope with standard deviation $\sigma = \ell_c/4$. See Fig. 2-3. Then, we correlate the

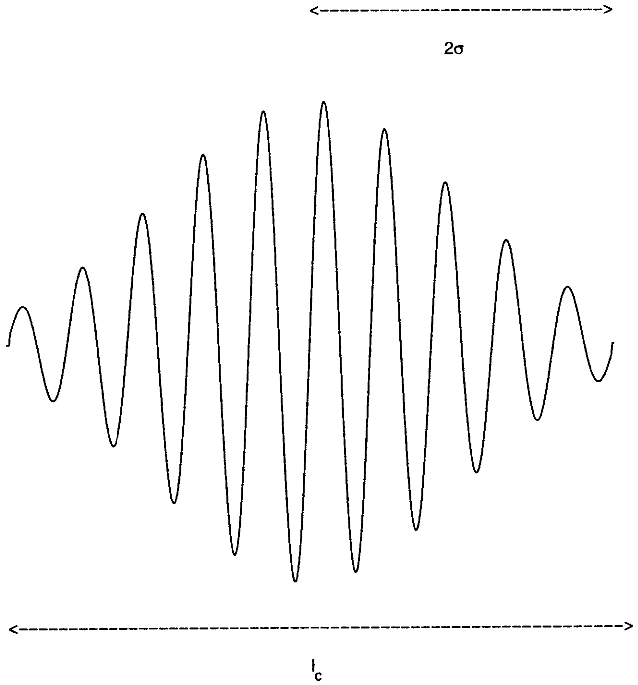

Figure 2-3: Wave packet $W(\mathbf{x}/\ell_c,\phi)$ with the extent of the packet $\ell_c = 4\sigma$. Note that ϕ is the orientation of the plane wave in the planar direction (the plane perpendicular to the page).

wave packet with local topography $h(\mathbf{x})$ within a box size of ℓ_c.

$$C(\mathbf{x}, \phi;\, \ell_c) = \left| \int_{|\mathbf{x}'-\mathbf{x}| \leq \ell_c/2} \mathrm{d}\mathbf{x}'\, W_{\ell_c}(\mathbf{x}' - \mathbf{x}, \phi)\, h(\mathbf{x}') \right| \tag{2.3}$$

For a chosen location $\mathbf{x}$ and $|\mathbf{k}|$ (or λ), $C(\mathbf{x}, \phi; \ell_c)$ computed at scale ℓ_c only depends on ϕ. For anisotropic surface, $C(\phi)$ should be predominantly π-periodic in ϕ, at each location $\mathbf{x}$. See Fig. 2-5 for an example of $C(\phi)$ calculated from the topography shown in Fig. 2-4. Then, the angular orientation of $\mathbf{a}(\mathbf{x})$ is defined to be perpendicular to the phase of the π-periodic part of $C(\phi)$ and is related to the local dominant wavevector $\mathbf{k}(\mathbf{x})$ of the topography. To obtain the phase of the π-periodic part, we compute:

$$Z = \int_0^{2\pi} e^{-2\phi i}\, C(\phi)\, \mathrm{d}\phi. \tag{2.4}$$

with $\mathbf{a}(\mathbf{x})$ derived from Z by:

$$\mathbf{a}(\mathbf{x}) = [-\Im(Z), \Re(Z)] \quad \text{and} \quad \mathbf{a}(\mathbf{x}) \perp \mathbf{k}(\mathbf{x}) \tag{2.5}$$

or simply let $|\mathbf{a}| = |Z|$ with the orientation of $\mathbf{a}$ orthogonal to that of Z.
Formally, this can be conceptualized as a nonlinear transform $\mathcal{A}_{\ell_c}[h(\mathbf{x})]$ of the elevation $h(\mathbf{x})$ to obtain a new field $\mathbf{a}(\mathbf{x}; \ell_c)$ for a particular choice of wavelength λ of the wave packet (used in the transformation). Note that this is defined at a length scale ℓ_c.

To obtain a measure for large scale topographic structures, we compute the "real" slope $\mathbf{s}(\mathbf{x}; L_s)$ at location $\mathbf{x}$ averaged over a length scale L_s:

$$\mathbf{s}(\mathbf{x}; L_s) = \langle \nabla h(\mathbf{x}) \rangle_{L_s} \tag{2.6}$$

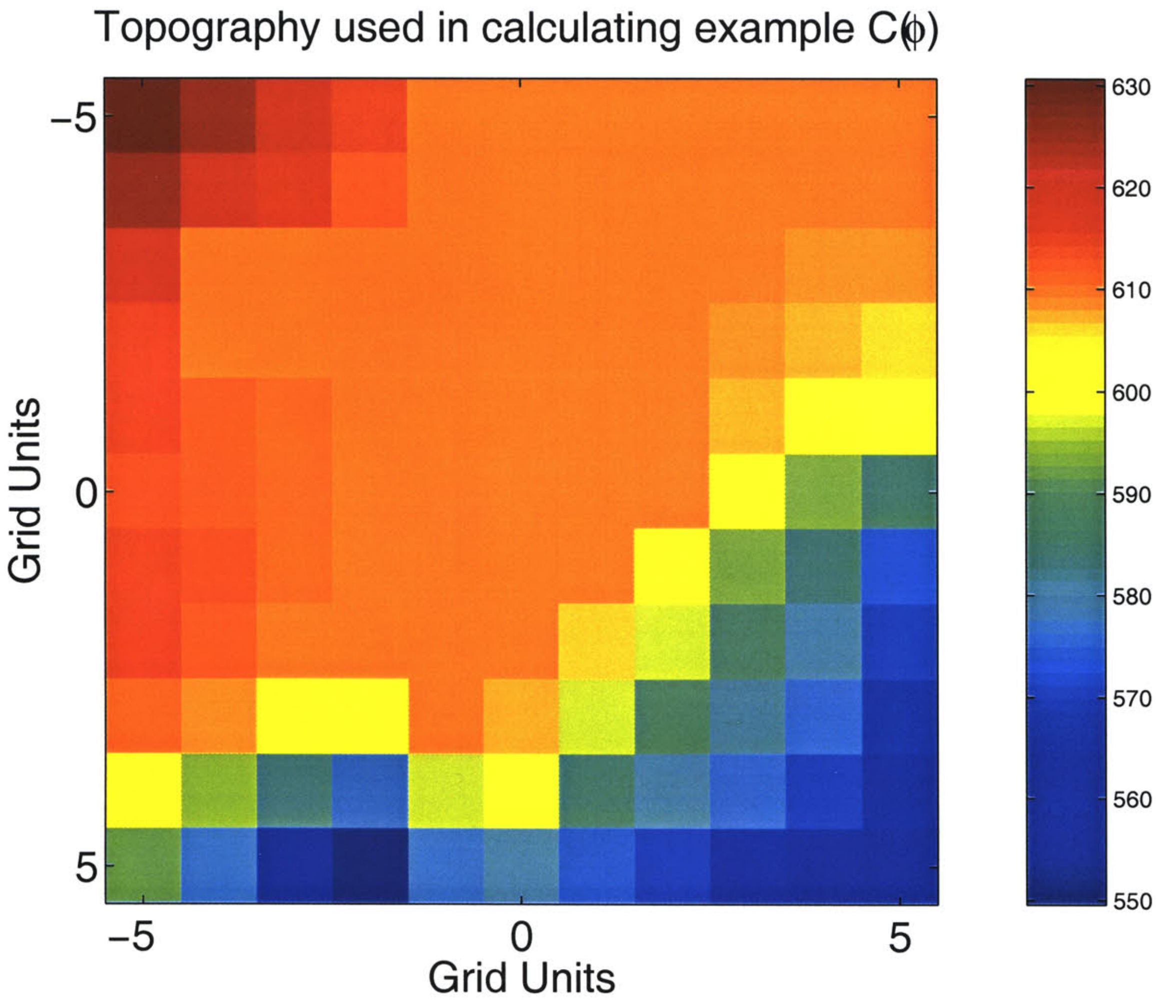

Figure 2-4: Example topography for calculating $C(\phi)$

The average is taken as followed:

$$\langle \nabla h(\mathbf{x}) \rangle_{L_s} = \frac{\int_{|\mathbf{x}'-\mathbf{x}|\le L_s/2} d\mathbf{x}' g\left(\frac{\mathbf{x}'-\mathbf{x}}{L_s}\right) |\nabla h(\mathbf{x}')| \hat{\mathbf{s}}}{\int_{|\mathbf{x}'-\mathbf{x}|\le L_s/2} d\mathbf{x}' g\left(\frac{\mathbf{x}-\mathbf{x}'}{L_s}\right)} \tag{2.7}$$

where

$$g\left(\frac{\mathbf{x}-\mathbf{x}'}{L_s}\right) = \frac{1}{L_s^2} \exp\left[-8\left(\frac{\mathbf{x}-\mathbf{x}'}{L_s}\right)^2\right] \tag{2.8}$$

We expect the local dominant (preferred) direction of flow to be related to $\mathbf{s}(\mathbf{x}; L_s)$.

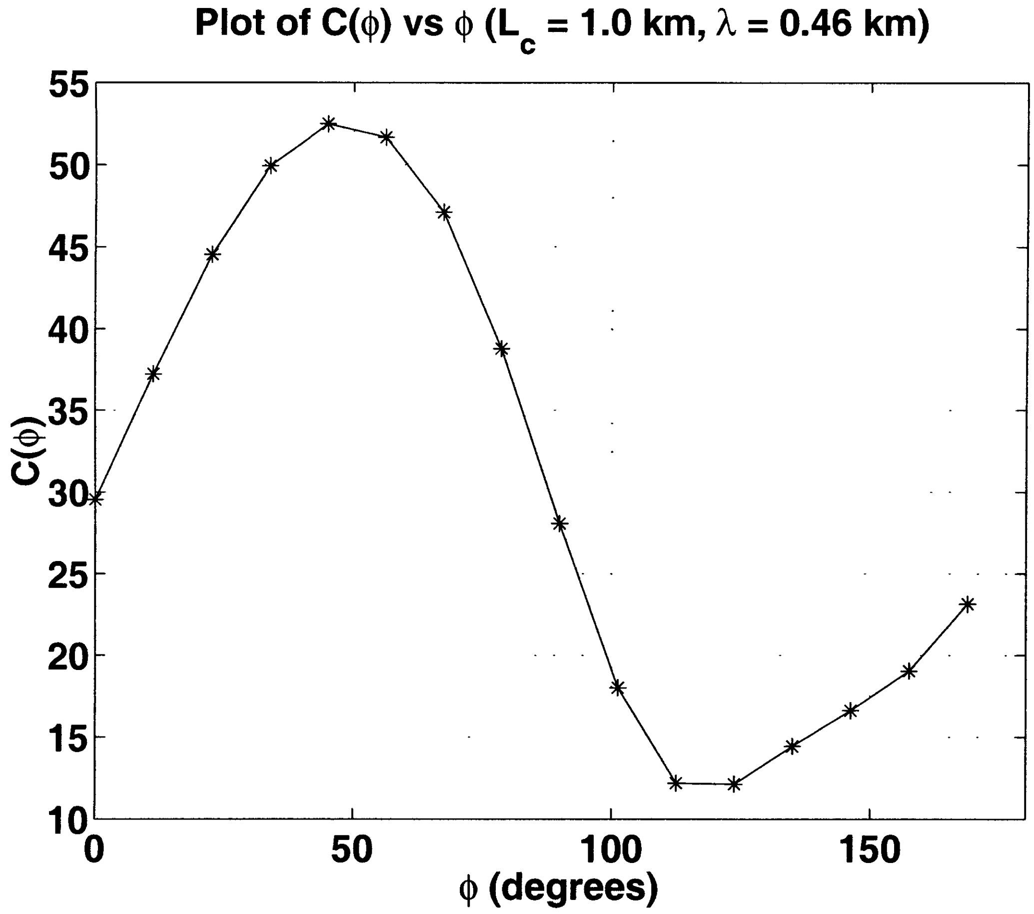

Figure 2-5: Plot of $C(\phi)$ computed for the topography shown in Fig. 2-4

2.3 Correlation between small and large scale structures

To answer our previous question about the correlation between small and large scale structures, we need to examine the correlation between **a** and **s** computed at different scales. Specifically, we want to know if $\mathbf{a}(\mathbf{x};\ell_c)$ is parallel (or anti-parallel) to $\mathbf{s}(\mathbf{x};L_s)$, and if so, at what relative scales? At each point in space, we compute the angular difference between the two vectors:

$$\delta\theta(\mathbf{x};\, L_s, \ell_c) = \cos^{-1}\left\{\frac{|\mathbf{a}(\mathbf{x};\ell_c)\cdot\mathbf{s}(\mathbf{x};L_s)|}{|\mathbf{a}|\ |\mathbf{s}|}\right\} \tag{2.9}$$

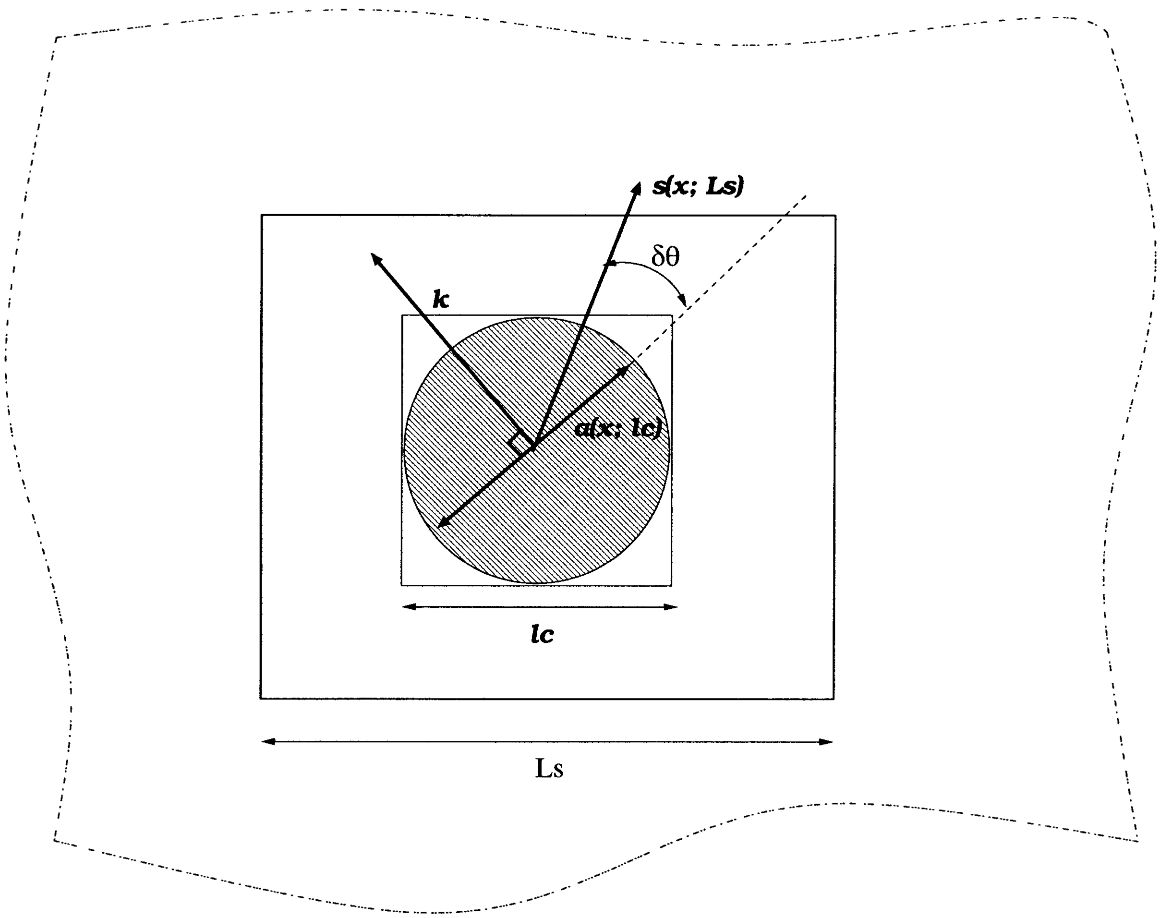

Figure 2-6: Diagram showing boxes (with sizes ℓ_c and L_s) within which **a** and **s** are computed. The angular separation between them is labelled $\delta\theta$. Note that **a** is defined to be perpendicular to the local dominant wavevector **k** and **a** is indistinguishable from $-\mathbf{a}$.

See Fig. 2-6 for a clarification. From this, we can calculate various statistics such as,

$$\text{Prob}(\delta\theta), \quad \langle\delta\theta\rangle, \quad \langle(\delta\theta)^2\rangle, \quad \langle\cos^2(\delta\theta)\rangle, \quad \text{etc.} \tag{2.10}$$

as a function of ℓ_c and L_s (and λ), where $\langle\rangle$ is an average over the spatial domain of interest.

We pay special attention to the following statistics (or correlation function) in our analysis:

$$\langle\cos^2\delta\theta\rangle$$

which is the average cosine squared of the angular separation of **a** and **s**, and

$$W = \frac{\langle |\mathbf{a}.\mathbf{s}|^2 \rangle}{\langle |\mathbf{a}|^2 |\mathbf{s}|^2 \rangle} = \frac{\langle |\mathbf{a}|^2 |\mathbf{s}|^2 \cos^2 \delta\theta \rangle}{\langle |\mathbf{a}|^2 |\mathbf{s}|^2 \rangle}.$$

which is the weighted average cosine squared of the angular separation by the magnitude $|\mathbf{a}|^2$ and $|\mathbf{s}|^2$.

2.4 Note on computing $\mathbf{a}(\mathbf{x}; \ell_c)$

It is known in signal processing that if a time series has an unambiguous linear trend, the resulting power spectrum will be a power law decay of $S(k) \sim k^{-2}$. This can be easily seen when we consider the Fourier coefficients in the following function:

$$f(x) = \begin{cases} kx, & \text{for } 0 \leq x \leq a \\ 0, & \text{otherwise.} \end{cases}$$

where k and a are constants. The magnitude of the Fourier coefficients will decay as $\sim 1/n^2$ with higher harmonics parameterized by increasing n. A signal with a linear trend can be regarded as the sum of a function like $f(x)$ and a part without a linear trend (which contains the small scale structures of the original signal). As a result, the statistics of the small scale structures and fluctuations revealed by the power spectrum (or correlation analysis) can be obscured by the contribution from the overall trend. This will not be desirable in studying local anisotropy. To remedy this, we detrend locally our topography by subtracting from it the best fitting plane:

$$\begin{aligned} \min_{\{a,b\}} \chi^2 &= \sum_{\mathbf{r} \in R} [h(\mathbf{r}) - f(\mathbf{r}; a, b)]^2, \quad \text{where } f(\mathbf{r}; a, b) = ax + by + c. \\ h'(\mathbf{r}) &= h(\mathbf{r}) - f(\mathbf{r}; a, b). \end{aligned} \tag{2.11}$$

which we find by χ^2 least square fitting in 2 dimensions.

2.5 Tests on isotropic synthetic topography

As a control, we would like to apply our methodology in correlating local anisotropy $\mathbf{a}$ with local slope $\mathbf{s}$ to a synthetic isotropic self-affine topography. The basic technique to generate such topography is to convolve Gaussian noise $\eta(\mathbf{x})$ with a kernel $G(\mathbf{x})$ such that the resulting signal possesses an algebraic power spectrum. ie. $h(\mathbf{x}) = \sum_{\mathbf{x}'} G(\mathbf{x}-\mathbf{x}')\eta(\mathbf{x}')$ with $\hat{h}(\mathbf{k}) \sim \mathbf{k}^{-\beta}$. We follow the algorithm indicated by [12]:

1) Generate an $N \times N$ square grid consisting of N^2 equally spaced points of Guassian random variables η_{mn}.

2) A two-dimensional discrete Fourier transform is taken:

$$\hat{\eta}_{st} = (1/N)^2 \sum_{n=0}^{N-1} \sum_{m=0}^{N-1} \eta_{mn} \exp\left[-\frac{2\pi i}{N}(sn+tm)\right]$$

generating an $N \times N$ array of complex coefficients $\hat{\eta}_{st}$.

3) A fractal dimension D is specified with the corresponding exponent β given by $D = (7-\beta)/2$. The Fourier coefficients are then filtered as followed:

$$H_{st} = \hat{\eta}_{st}/k_r^{\beta/2}$$

4) An inverse two-dimensional Fourier transform is performed to obtain $h(\mathbf{x})$.

The topography used in the testing is shown in Fig. 2-7. We choose a fractal dimension of about 2.1.

Since this is isotropic, we expect to see no correlation of $\mathbf{a}$ and $\mathbf{s}$. As suspected, we discover that the angular separation between $\mathbf{a}$ and $\mathbf{s}$ is randomly distributed with no correlation at all scales L_s with which we compute our $\mathbf{s}$. Fig. 2-8 is a histogram showing the distribution of $\delta\theta$ with different L_s, but with ℓ_c fixed at 21 grid units.

Fig. 2-9 shows how $\langle \cos^2 \delta\theta \rangle$ varies with L_s, again with ℓ_c fixed at 21 grid units. Remember that $\langle\rangle$ is a spatial average over the topography. As the plot shows, the

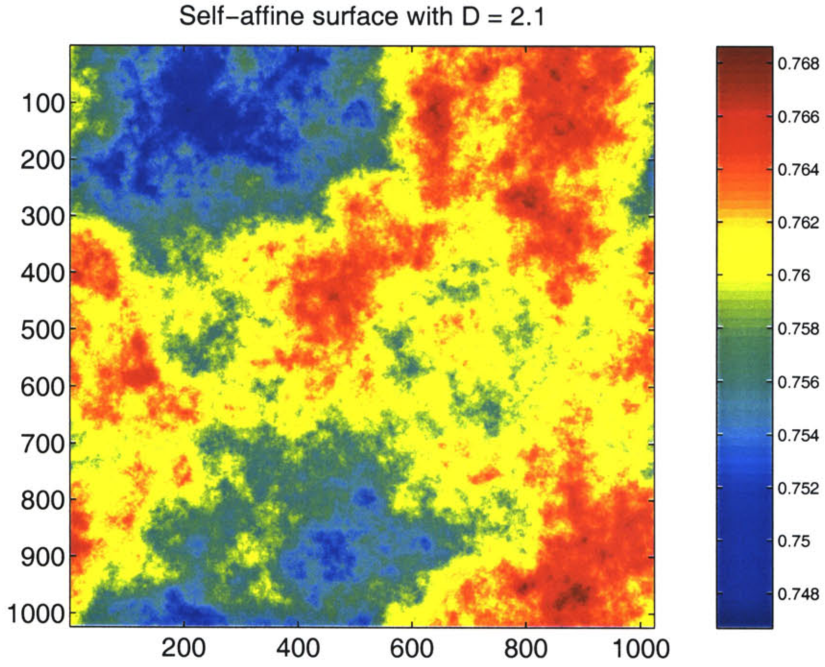

Figure 2-7:

$\langle \cos^2 \delta\theta \rangle$ fluctuates around 0.5, indicating a random distribution over all possible angles.

This result indicates that any deviation away from uniform distribution of $\delta\theta$ is significant and comes from the genuine anisotropic nature of the surface.

2.6 Tests on a synthetic inclined anisotropic surface

As a further understanding of the characteristics of the correlation between **a** and **s**, we apply the method to an "ideal" slope. This is an inclined anisotropic surface with $C(x_\perp) > C(x_\parallel)$. See Fig. 1-1. The algorithm for generating this surface is exactly the same as for the isotropic case, except that in filtering the Fourier coefficients, the following is done:

$$H_{st} = \hat{\eta}_{st}/(k_x^2 + Ak_y^2)^{\beta/4}$$

where A is the controlling parameter for the degree of anisotropy.

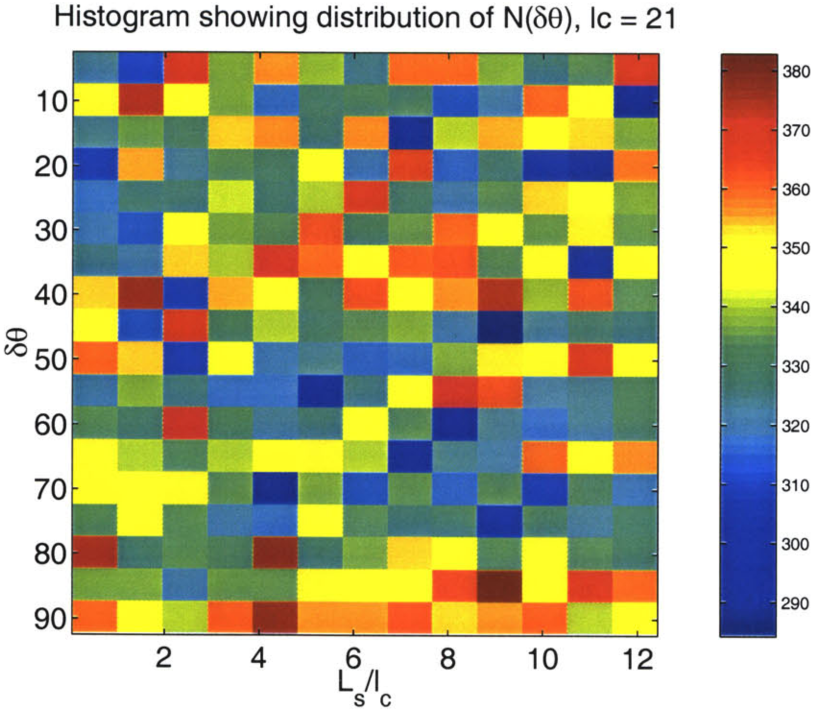

Figure 2-8: For synthetic isotropic self-affine surface with $D = 2.1$

Fig. 2-10 shows the inclined surface we used. It is made smoother in the dip ($x_{\|}$) direction than the strike ($x_{\perp}$) direction. This is the prediction of the linear theory of stochastic anisotropic diffusion and it is almost always observed in real topography. To check that the topography we generated is anisotropic, we calculate its height-height correlation function $C(x)$ in both the dip and strike direction. The result is shown in Fig. 2-11.

Notice that $C(x_{\perp}) > C(x_{\|})$. We would like to see how **a** correlates with **s**. We apply our method of extracting **a** from local transforms, and study how $\langle \cos^2 \delta\theta \rangle$ changes with L_s. The result is presented in Fig. 2-12. We can clearly see that **a** measured at $\ell_c = 21$ becomes more and more correlated with **s** measured at larger and larger L_s. The simplest explanation is that the anisotropic orientation has been set to line up with the direction of the inclined plane (dip). When you measure **s** at a scale smaller than the system size, in addition to the global slope direction, you will also pick up local fluctuations. The smaller the scale with which you measure your slope, the more significant the local fluctuations become. Therefore, the correlations

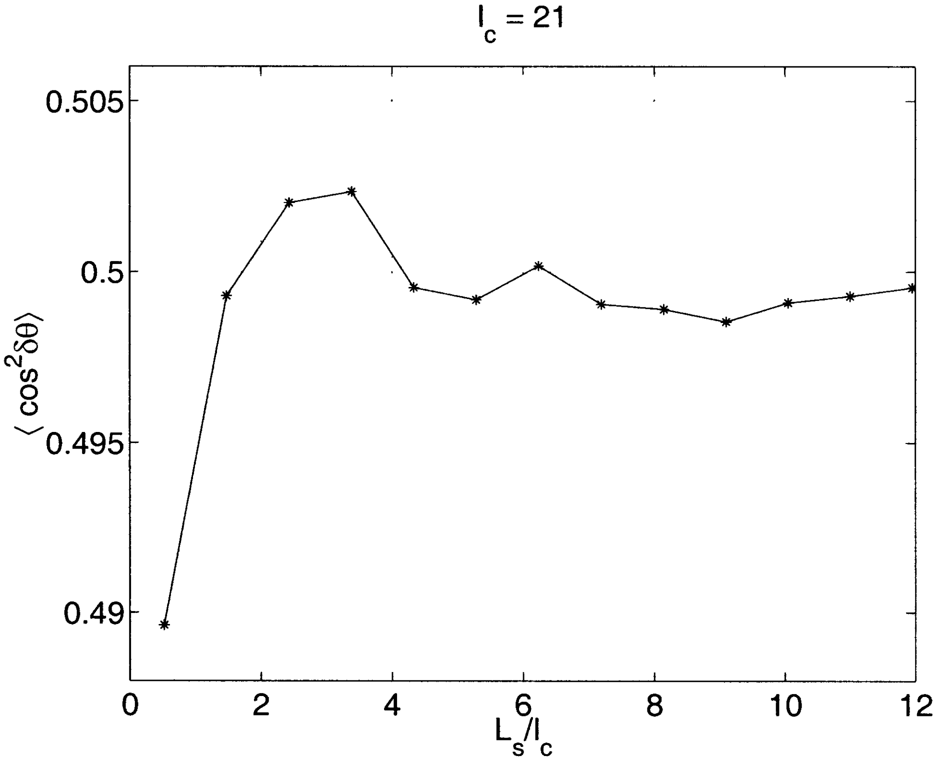

Figure 2-9: For synthetic isotropic self-affine surface with $D = 2.1$

will not be high when L_s is much smaller than the system size.

This exercise has shown empirically that our method of local transforms in measuring local anisotropy **a** and local slope **s** can indeed yield useful information about how one correlates with the other at different scales.

See Appendix C for the local anisotropy director field measured for a set of plane waves and a pattern of stripes and bands.

2.7 Some details on artefacts due to discretization, finite domain, etc

It can be shown that the various numerical artefacts due to discretization, finite limit of integration (in performing local transforms), etc., are remedied when $\ell_c/\lambda \geq 10$ is ensured. The details of calculations and analysis can be found in Appendix A.

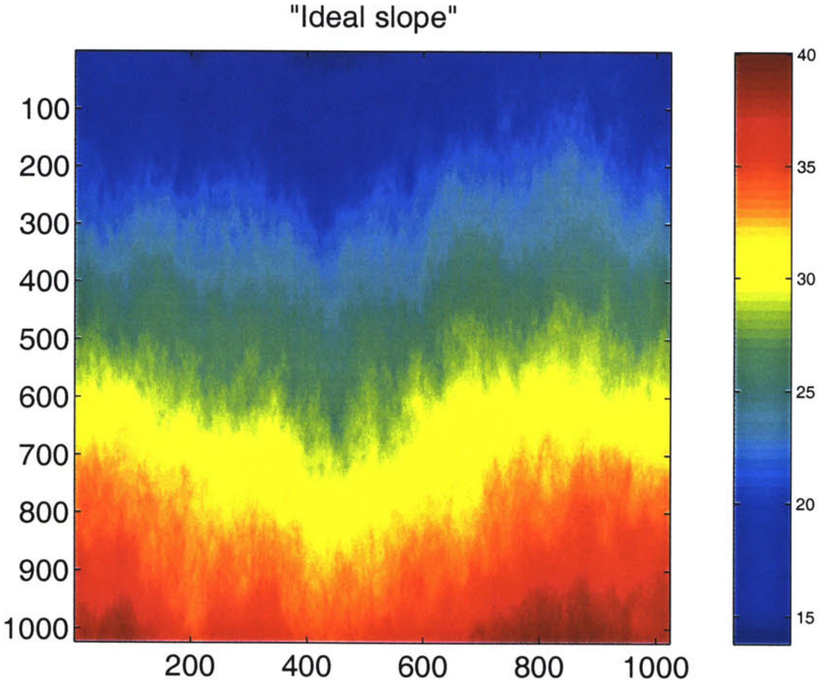

Figure 2-10:

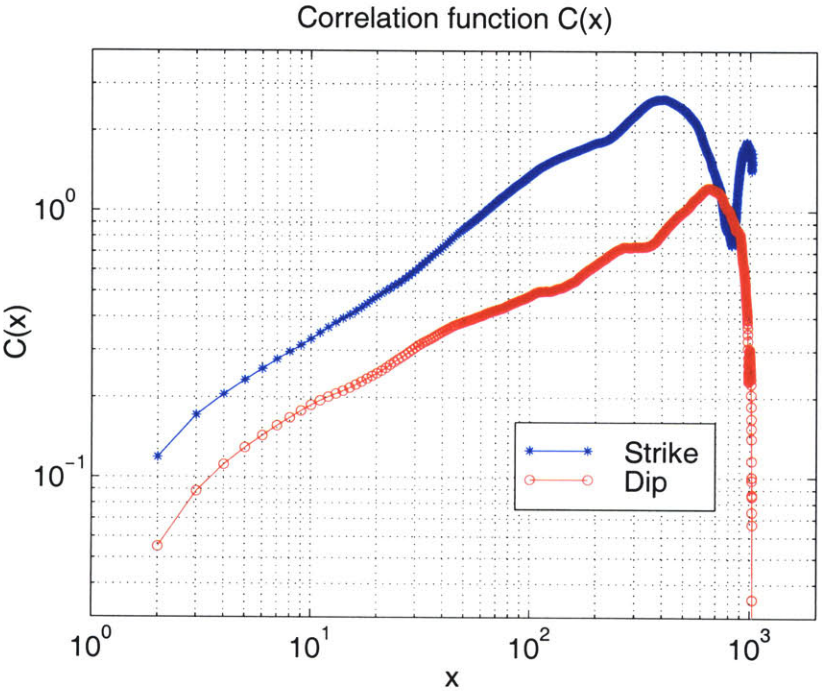

Figure 2-11: For a synthetic inclined anisotropic surface. Note: dip is in the direction of steepest descent and strike is the direction parallel to it and that $C(x_\perp) > C(x_\parallel)$

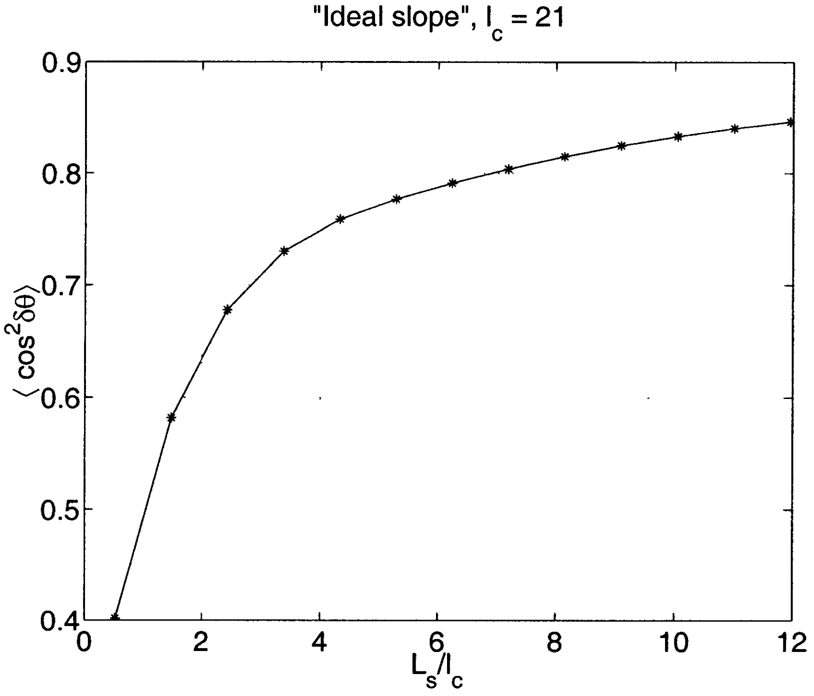
"Ideal slope", l_c = 21
0.9
0.8
0.7
0.6
0.5
0.4
$\langle \cos^2\delta\theta \rangle$
0
2
4
6
8
10
12
L_s/l_c

Figure 2-12: .

Chapter 3

Results

3.1 Results from empirical studies

Topographical data is obtained from the USGS online database. The 1-degree Digital Elevation Models (DEM) is used which provides coverage in 1- by 1- degree blocks. It consists of a regular array of elevations referenced horizontally on the geographic (latitude/longitude) coordinate system of the World Geodetic System 1972 Datum (WSG 72) or the World Geodetic System of 1984 (WGS 84). There are 1200×1200 sample elevations in each block. We use linear interpolation to obtain an evenly spaced square grid of data in rectangular coordinate. In projecting the data from spherical to rectangular coordinate, we commit systematic errors which we can show to be negligible for our purposes. Details can be found in Appendix B.

We study a piece of topography that ranges from 38^o–39^o north latitude and 120^o–121^o west longitude, a rectangular area whose dimensions are roughly 100 km on a side, with a resolution of approximately 90 m. This area, entirely contained within California, ranges from the western flank of the Sierra Nevada mountains to the eastern edge of the Central Valley. (Fig. 3-1). Our area of interest contains a drainage basin with an unambiguous dominant slope (or direction of flow), and network of rivers can be seen to flow downhill in mostly one direction. A wide range of erosive features exist, including those of glacial, fluvial, and alluvial origin. The field of anisotropic director field is shown in Fig. 3-2. We compute $\langle \cos^2 \delta\theta \rangle$ for different relative scale L_s/ℓ_c at $\ell_c = 1.0$ km. The result is shown in Fig. 3-3. We discover that $\mathbf{a}$ measured at small scale $\ell_c = 1.0$ km is most strongly correlated with the slope $\mathbf{s}$ measured at $L_s \sim 10$ km $> \ell_c$. To convince ourselves that for L_s in this vicinity, $\mathbf{a}$ and $\mathbf{s}$ are most probably lined up, we examine the distribution of $\delta\theta$ for the case of $\ell_c = 1$ km and $L_s^* = 10$ km. See Fig. 3-4. This clearly indicates that the most probable $\delta\theta \sim 0^0$. This shows anisotropy measured at small scale ℓ_c is most correlated with large scale topographic features at L_s^*. In addition, we also examine a synthetic isotropic landscape with cross-section fractal dimension of $d_f = 1.2$. We find no such correlation and $\delta\theta$ is distributed at random as expected.

Finally, we examine the dependence of $\langle\cos^2\delta\theta\rangle$ on L_s for different ℓ_c. The result is shown in Fig. 3-5. Note that some of the curves have been displaced vertically to allow a clear comparison. It is observed from all the plots that local anisotropies calculated at scale ℓ_c are always most strongly correlated with local slope (or direction of dominant flow) measured at a larger scale L_s. We define this "optimum" length scale as L_s^*. On closer examination of Fig. 3-5, we discover that L_s^* increases monotonically with ℓ_c. We make a plot showing this in Fig. 3-6. It is found that when fitted to a power law, it has a very weak exponent which leads us to postulate $L_s^* \sim \log \ell_c$. This may be related to the fact that surficial erosion operates over a range of length scales rather than a distinct characteristic scale.

In a more general framework, the local slope (dominant direction of flow) can be regarded as a "stress" on the system and the local anisotropy as the "response" to this directional "stress". The results show that in the case of natural landscapes, the "response" is always correlated with a certain overall "stress" defined over a large scale.

However, the physical interpretation and significance of L_s^* and its relation to the local features of topography need to be examined more closely. This will be elucidated in the next chapter. Future investigation using this method can also provide a chance to study the "up-down" (a)symmetry of fluvial erosion, ie. to investigate if erosion at a point on a hillslope is more correlated with processes in the upstream or the downstream direction.

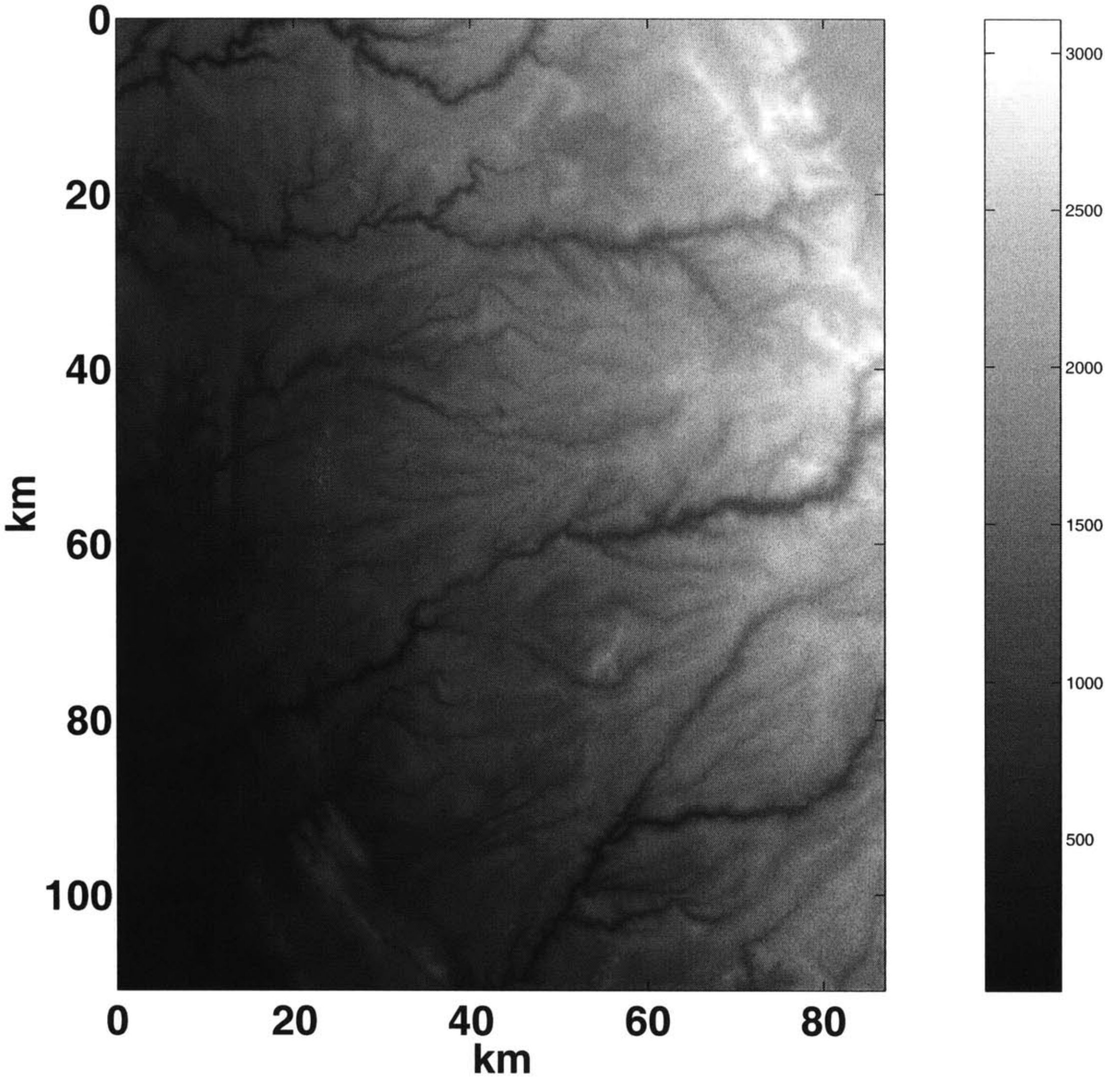

Figure 3-1: Topography used in this study. Data is obtained from USGS 1-degree DEM which ranges from 121°W/39°N to 120°W/38°N.

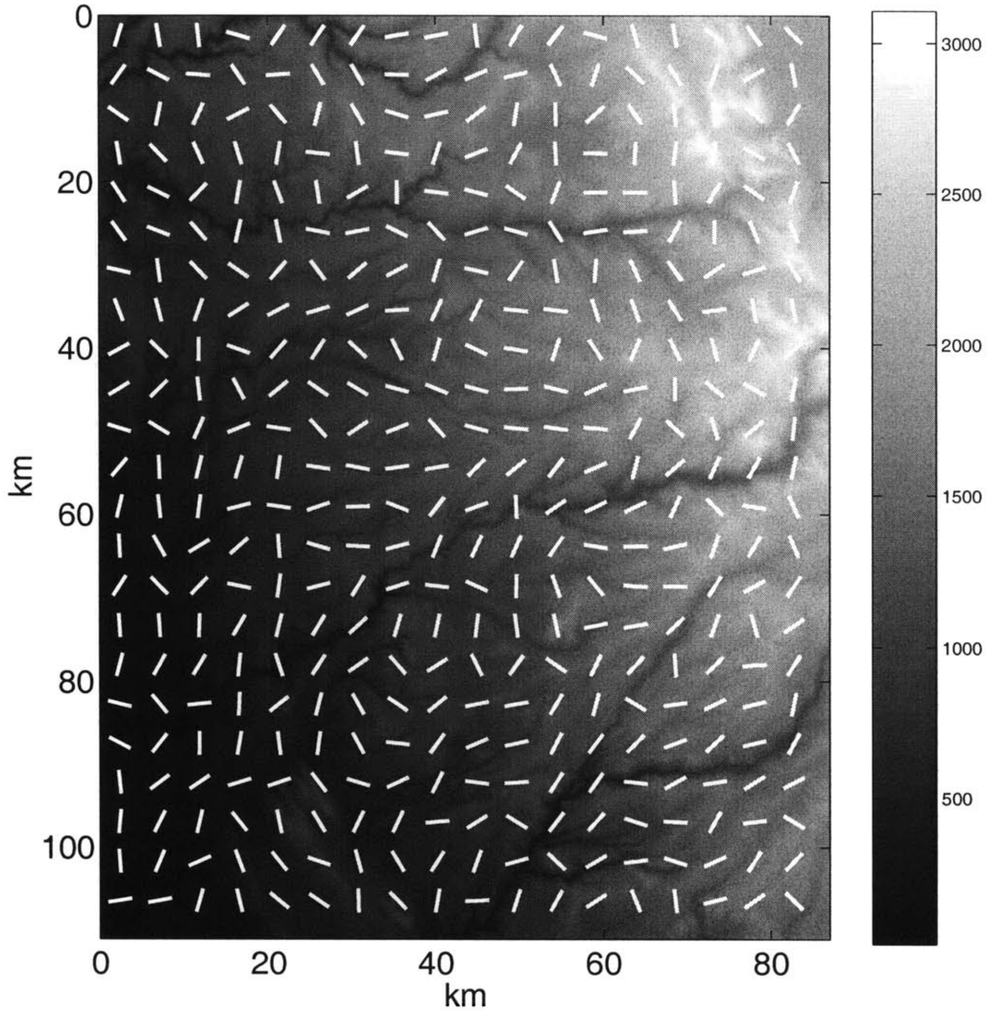

Figure 3-2: Anisotropic director field for the topography (121°W/39°N to 120°W/38°N).

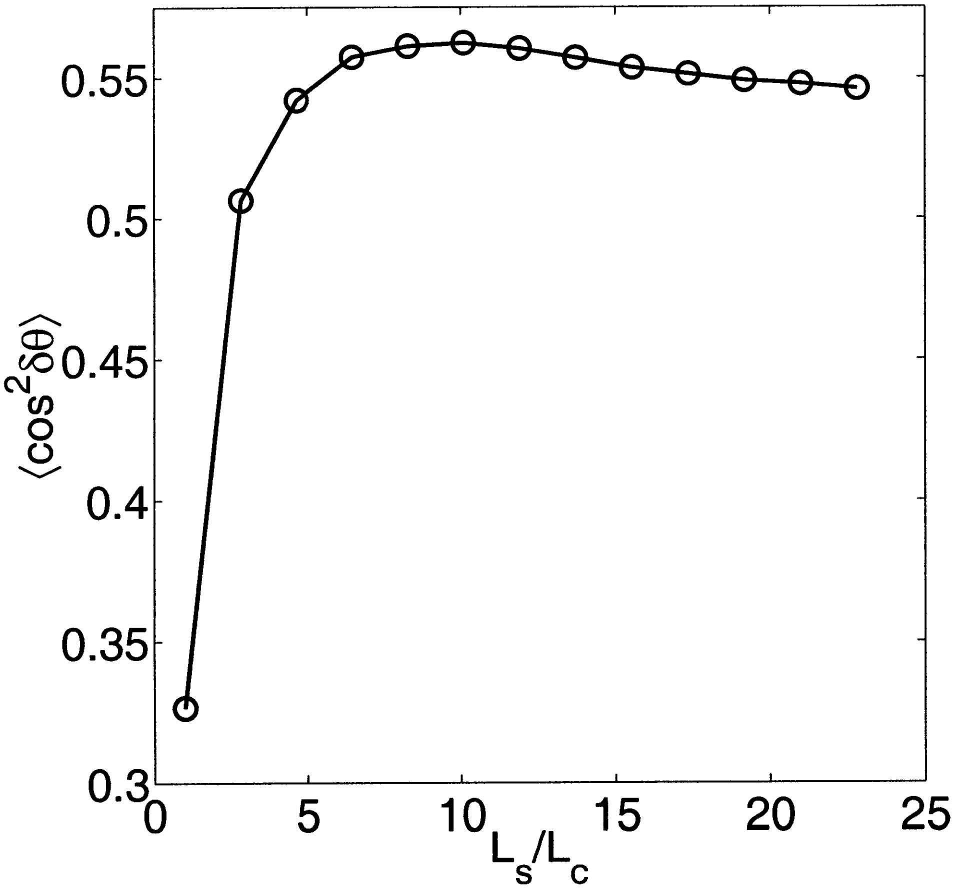

Figure 3-3: The average cosine square of the angular separation of **a** and **s** vs relative scales L_s/ℓ_c. This shows that the apparent dip direction **a** at small scale $\ell_c = 1$ km is most strongly correlated with the slope $\mathbf{s} = \langle \nabla h \rangle$ measured at $L_s^* \sim 10$ km $> \ell_c$.

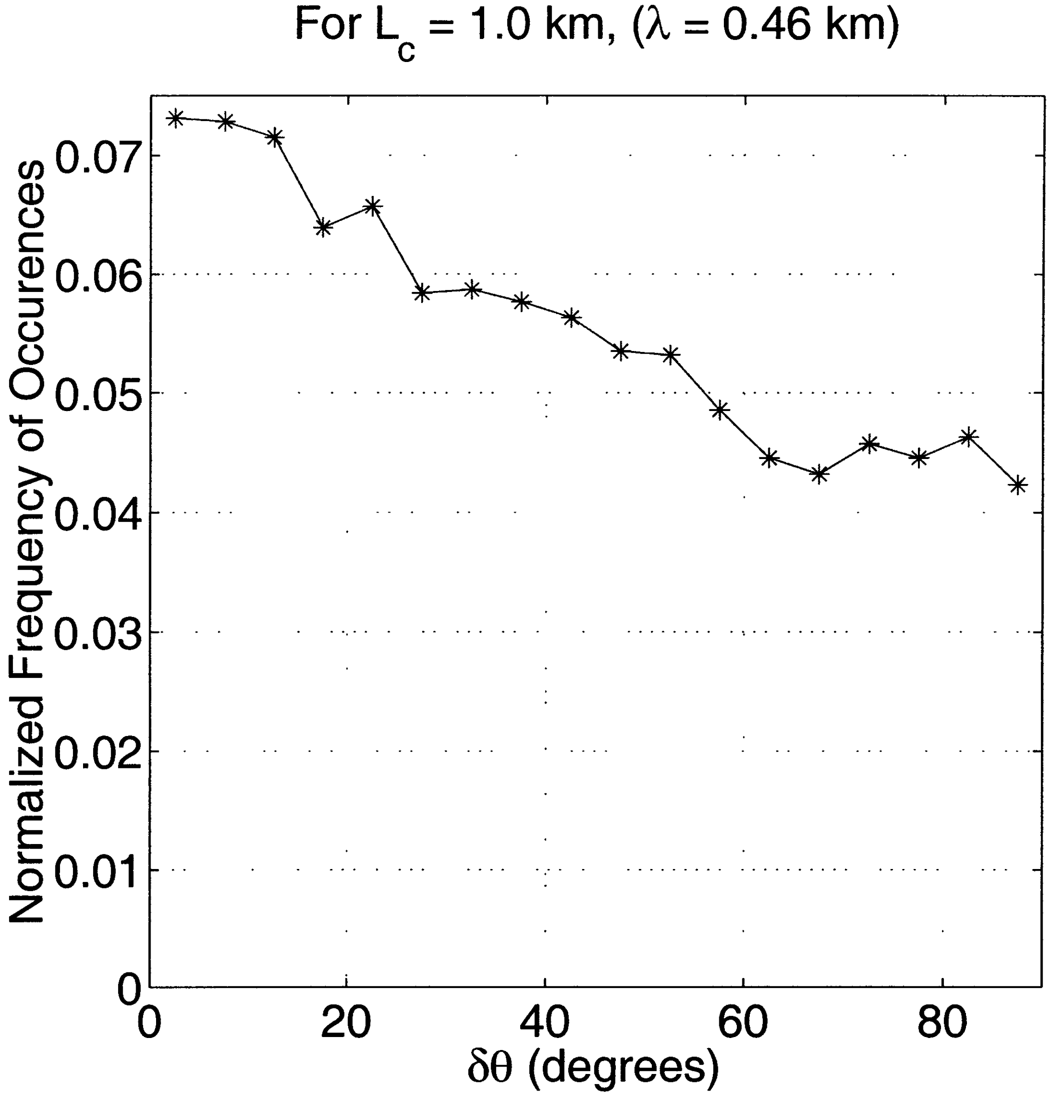

Figure 3-4: This shows the distribution of the angular difference $\delta\theta$ between the apparent dip direction **a** measured at small scale $\ell_c = 1$ km and the slope **s** measured at large scale $L_s^* = 10$ km. It indicates that the most probable $\delta\theta \sim 0^0$.

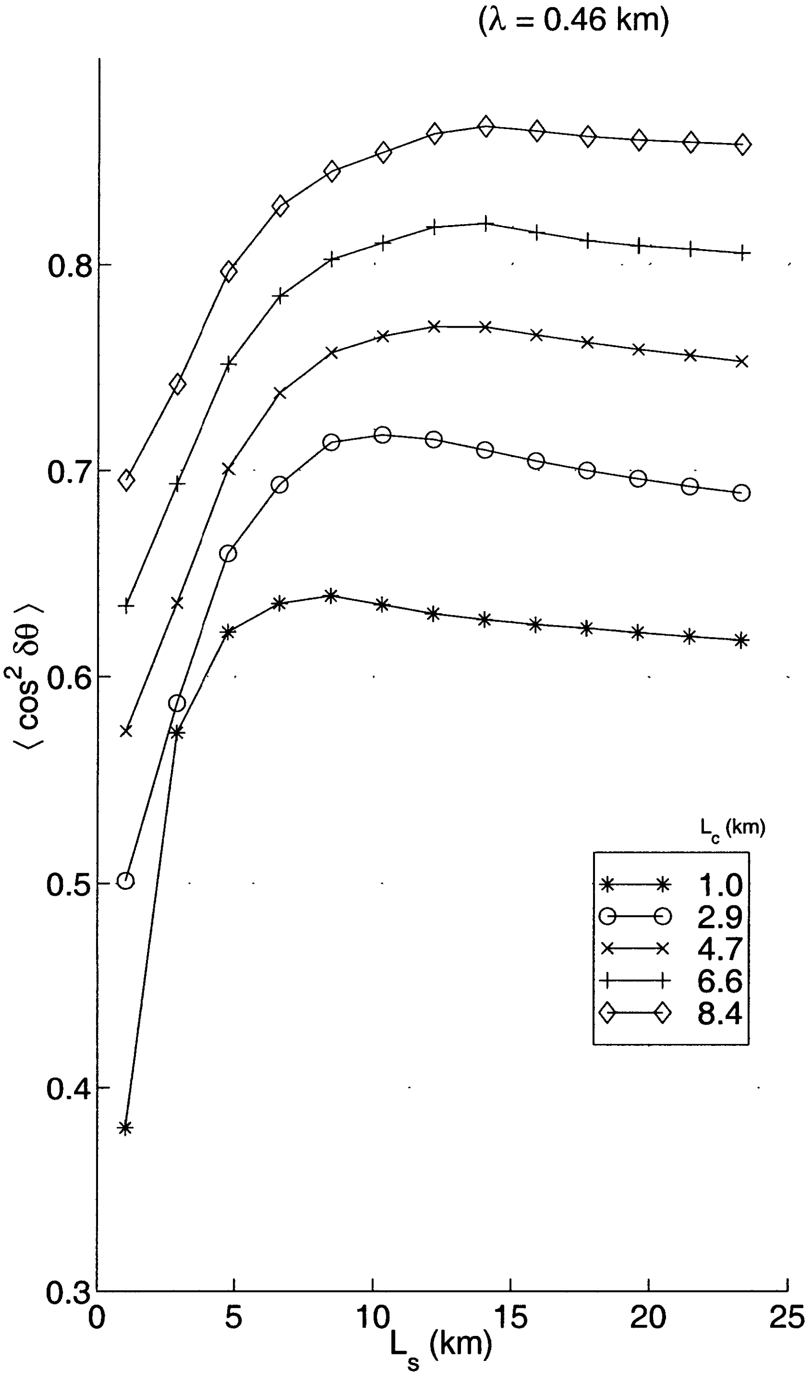

Figure 3-5: Plotting $\langle \cos^2 \delta\theta \rangle$ for various ℓ_cs. L_s^* is the length scale at which the correlation becomes optimum. Here we see that $L_s^* \sim$ 8–15 km for all values of ℓ_c.

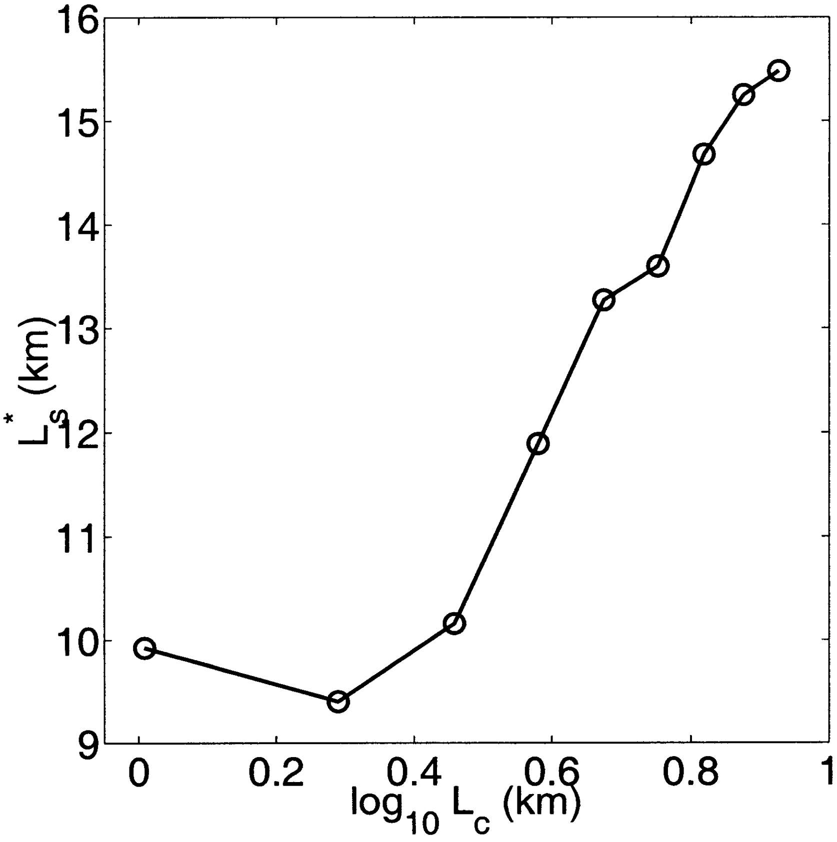

Figure 3-6: A plot of the optimal large scale L_s^* vs $\log \ell_c$ (Log of length scale at which $\mathbf{a}$ is measured). This shows approximately $L_s^* \sim \log \ell_c$ for large ℓ_c.

Chapter 4

River Drainage Basins

4.1 Fractal river basins and networks

When water flows across a landscape from the drainage source to outlet, it does so in channelized networks. With the availability of digital elevation maps (DEM), it becomes possible to extract the drainage pattern of a large river network over an extended area (typically in the order of hundreds to thousands of kilometres). This enables a study of the structure and scaling properties of such fields and networks. The most striking feature of such networks is that they are fractal in nature [7]. It is very difficult to tell the difference between the Amazon and the little creek in your backyard without a scale bar. The most ubiquitous result is the power law distribution of the total contributing (drainage) area with exponent 0.43 [14]. It comes into perspective when we ask what L_s^*, the characteristic length scale at which **a** and **s** become optimally correlated, means in the light of this fractal nature of river networks. Ideally, if river network and topographic feature is truly fractal, one should be suspicious if our analysis has extracted a characteristic length. A purely fractal object by definition has no characteristic length scale. But things are not exactly fractal. In nature, one always have upper and lower cutoffs. The upper cutoff usually comes from the system size, or a finite size effect. Afterall, nothing on earth is infinite in extent. In the case of river network, the spatial extent of the entire drainage basin becomes a characteristic length scale. The self-similarity stops beyond this scale. For the Amazon, you would hit the oceans when you consider a larger length scale than the continent. The lower cutoff is at the other end of the spectrum. It can arise merely because physical entities go into the atomic realm after a certain size and our usual assumption of continuum does not hold and self-similarity breaks down. In the case of river networks, the cutoff is much higher and it has something to do with the different processes acting at different scales. For example, in the region where discharge is small, water movement is dominated by diffusional or dispersive, creep-like mass-wasting process. On the other hand, at places where discharge is great, advective or concentrative, fluvial process will be significant. Naturally, self-similarity will not hold across the treshold. In the following sections, we would like to demonstrate how the characteristic size of a drainage basin is related to L_s^* from our analysis.

4.2 Total contributing area A_i

We first discuss a concept called the total contributing area, or the drainage area, of a topography. One physical assumption involved is that the amount of rainfall is uniformly distributed over the landscape both in space and time, only allowing a very small variance. With this assumption, we can surrogate the discharge Q, which is a physical quantity, by the total contributing (drainage) area A, which is a geometrical or topological quantity,

$$Q \propto A \tag{4.1}$$

In short, we are trying to deduce the amount of discharge through a point by examining the topography around it.

The algorithm for computing A_i is very simple. The topography we are interested in computing this is first discretized on a rectangular grid (which is already done since we are using DEMs). Conceptually, place a ball on each point on the grid. From each point, you examine the nearest neighbors and pick the lowest point to which your ball "rolls" to. A counter is kept at each point to keep track of how many times a ball has passed through that point. The ball stops when it reaches a point of local minimum. The magnitude of the counter indicates the total contributing area at that point, which is the number of balls that passed through the point. We can express this idea more precisely. Let the total contributing area at the i^{th} site be A_i, then

$$A_i = \sum_{j \in nn(i)} W_{ij} A_j + 1 \tag{4.2}$$

where

$$W_{ij} = \begin{cases} 1, & \text{if } i,j \text{ are connected, that is, if } j \to i \text{ is a drainage direction} \\ 0, & \text{otherwise.} \end{cases} \tag{4.3}$$

Here, the index j spans the eight nearest neighbors with $nn(i)$ standing for the nearest neighbors to i. The matrix W is determined by the direction of steepest descent. Sites A and B are connected if the direction of steepest descent from A is in the direction of B. We can solve the system of equations for A_i:

$$A = (I - W^{\mathrm{T}})^{-1} r \tag{4.4}$$

where $r = \{1, 1, \cdots, 1\}$.

Physically, A_i is related to the total discharge through the point i. See Fig. 4-1

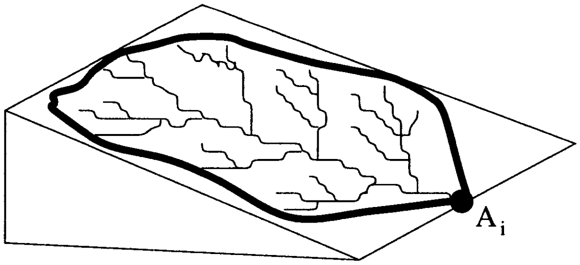

Figure 4-1: Total contributing area at a point, which is related to the characteristic area of the basin.

This can also be viewed as the characteristic area of the drainage basin. As mentioned in the previous section, the probability distribution of A_i was demonstrated

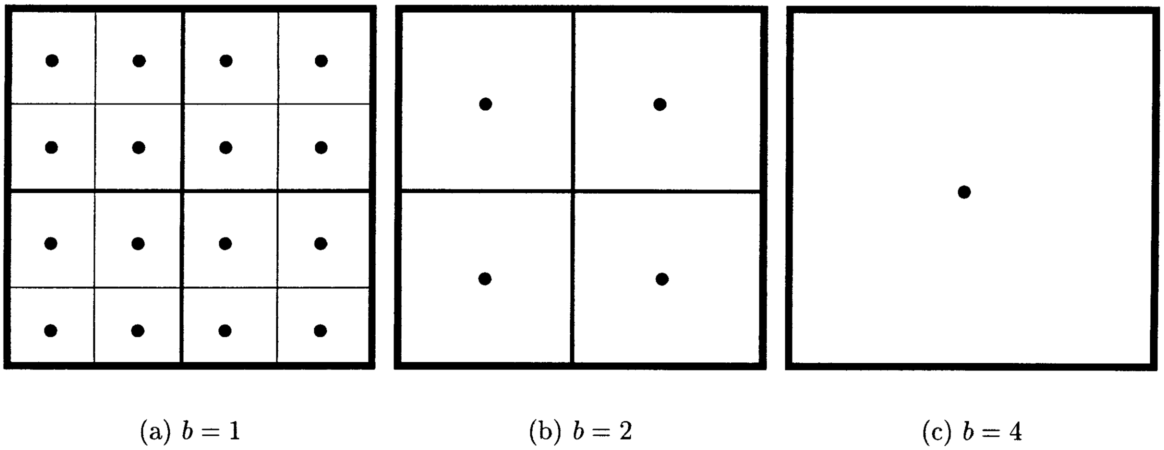
(a) $b = 1$ (b) $b = 2$ (c) $b = 4$

Figure 4-2: Figure showing the coarse graining scheme. At each step, the new grid point is taken to be the average of the neighboring cluster of 4 grid points forming the square

to exhibit power law behavior. To make the connection with our idea of calculating **a** over many different length scales ℓ_c, we need to examine A_i at different length scales also. One way of doing this is to coarse grain the topography and recompute A_i. We adopt a coarse graining scheme which preserves the main height of the topography. ie. replace a cluster of grid points by a single point computed from their average height. This idea is best elucidated in Fig. 4-2.

There is another way to examine the self-similarity of drainage networks. Instead of the probability distribution of the total contributing (drainage) area $P[A]$, it is often more convenient to examine the exceedence probability distribution $P[A \geq a]$, ie. the probability of contributing area bigger than a certain value a.

$$P[A \geq a] = \int_a^\infty P(A)dA \tag{4.5}$$

We examine $P[A \geq a]$ as we coarse grain our topography to varying degrees. The result is shown in Fig. 4-3.

For over two or three order of magnitudes, the distributions exhibit power law scaling behavior. The deviations from the power law behavior for large A_i are due to finite size effect. Note that in Fig. 4-3, the curves for the coarse grained topography

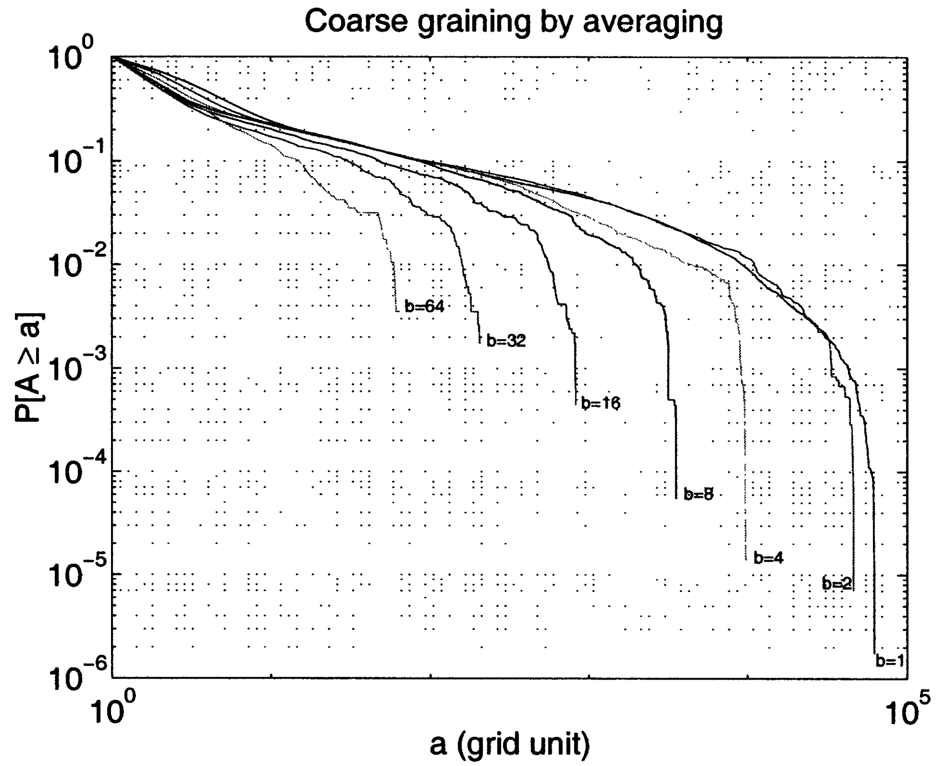

Figure 4-3: The study of the exceedence probability distribution of total contributing (drainage) A_i under different coarse graining scales b.

have not be rescaled to the same unit as the original, and therefore leading to different degrees of finite size cutoff. The unit used in this plot is the size of the lattice separation. In other words, the lattice size represents bigger actual length (eg. in km) for the more coarse grained topography. After proper rescaling, the curve should collapse on top of each other. We would like to compute the average contributing area $\langle A\rangle^{1/2}$ and examine how it changes under various degrees of coarse graining. Here, all grid units are normalized to be equivalent to that of the original DEM (1 grid unit = 92.764 m). In Fig. 4-4, we can observe that the average total contributing area increases as a function of b. We would like to make a direct comparison of $\langle A\rangle^{1/2}$ with our L_s^*, the optimum scales with which $\mathbf{a}$ and s become optimally correlated. In the previous section, we have established that L_s^* depends on the scale ℓ_c with which we measure $\mathbf{a}$. In analogy, $\langle A\rangle^{1/2}$ depends on the degree of coarse graining, or the length

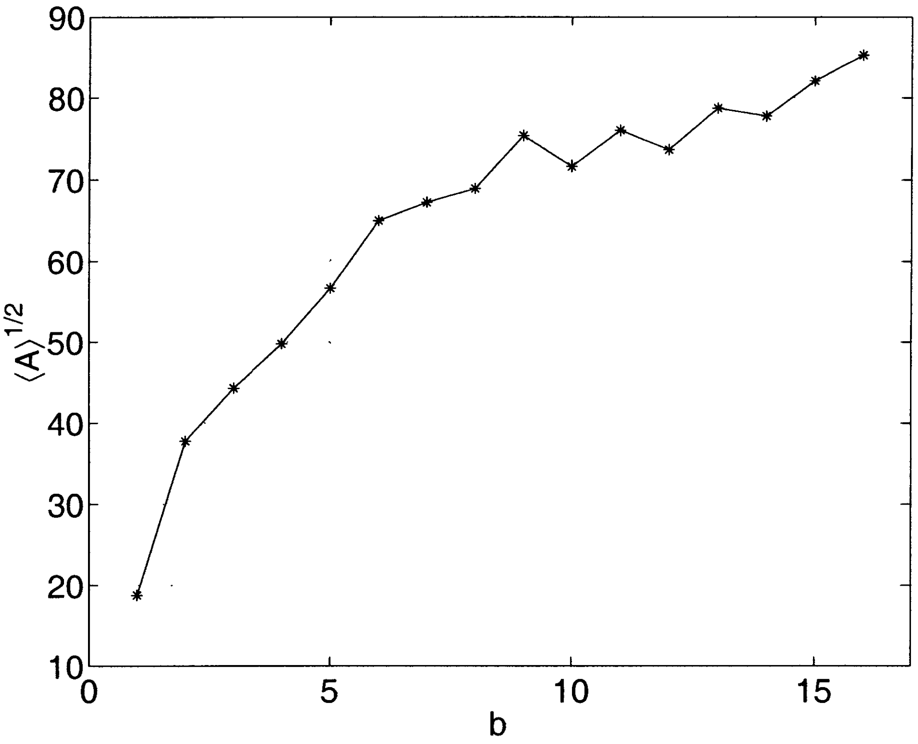

Figure 4-4: Study of the dependence of $\langle A \rangle^{1/2}$ on coarse graining.

scale at which you study the topography.

$$\begin{aligned} L_s^* &= L_s^*(\ell_c) \\ \langle A \rangle^{1/2} &= \langle A \rangle^{1/2}(b). \end{aligned} \tag{4.6}$$

In the above, b is being converted to an actually length. $b = 1$ corresponds to the original DEM, which translates to $b' = 92.764$ m, and $b = 2$ corresponds to $b' = 92.764 \times 2$ m $= 185.528$ m, and so on. Therefore, we can make a direct comparison between the two by plotting the length scale dependence together in one single plot.

Fig. 4-5 indicates that L_s^* is related to $\langle A \rangle^{1/2}$ the average contributing area in the topography. Therefore, L_s^* is closely related to the average basin size. Physically, this implies that local statistical anisotropy at a given point in the topography is, on the average, determined by the large scale structure in the order of the size of the drainage basin that discharges through the given point. This idea is pictorially

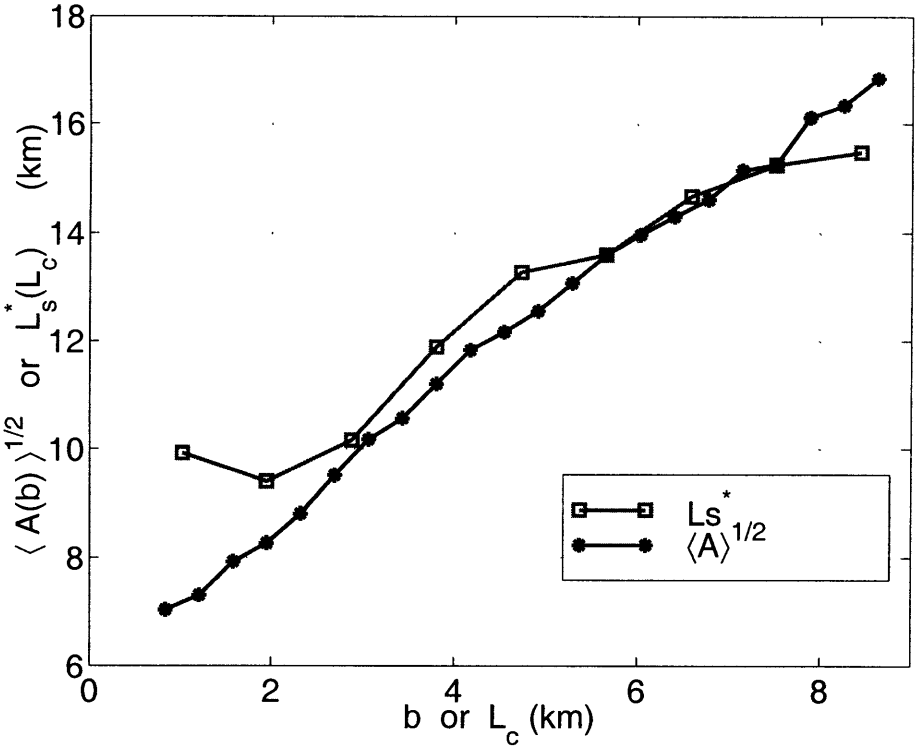

Figure 4-5: A comparison between L_s^* and $\langle A \rangle^{1/2}$ measured at different length scales. The topography is the same as the one used in the previous analysis.

summarized in Fig. 4-6

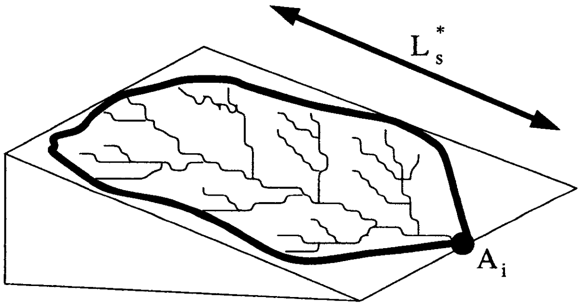

Figure 4-6: L_s^* is related to the length scale of the average drainage area $\langle A \rangle^{1/2}$, or the average basin size.

Chapter 5

Relocalization of Correlation Functions

5.1 Fluvial erosion processes

Thus far, two principal processes are identified to be at work during erosion which can be briefly described as diffusive and advective processes. In diffusive processes, the flux of sediment is dependent on the local slope ∇h of the topography and in simple diffusion, this flux is proportional to the local slope. On the other hand, advective processes may depend on the water discharge Q in addition to the slope. We can summarize these ideas mathematically as:

$$\frac{\partial h}{\partial t} = \nabla.(\mathbf{F}_1(\nabla h) + \mathbf{F}_2(Q, \nabla h)) + U \tag{5.1}$$

where U is the rate of tectonic uplift.

In region where there is active sediment production by fluvial erosion processes, the advective processes will dominate and happen at time scales much faster than diffusive and uplifte processes. The evolution of the land surface may be given by:

$$\frac{\partial h}{\partial t} = \nabla.\mathbf{F}_2(Q, \nabla h) \tag{5.2}$$

As mentioned in the previous chapter, assuming homogeneous rainfall over space and time, one can surrogate the total contributing area A for the water discharge Q and write

$$\frac{\partial h}{\partial t} = \nabla.\mathbf{F}(A, \nabla h) \tag{5.3}$$

dropping the subscript "2" in $\mathbf{F}_2$.

Studies have given support to the idea that the flux $\mathbf{F}$ of many geomorphic processes can be approximated as a power function of A and ∇h [13]:

$$\mathbf{F} \propto A^m s^n \tag{5.4}$$

where $\mathbf{s} = \nabla h$ and $\hat{\mathbf{s}}$ is the unit vector pointing in the steepest direction of descent. This empirical relation has been checked by many others.

5.2 Coupling total contributing area A_i to the slope s

We see that fluvial erosion is not solely determined by the slope $\mathbf{s}$ but also governed by A, the total contributing (drainage) area. Therefore, we ought to correlate our anisotropic director field $\mathbf{a}$ with function of both $\mathbf{s}$ and A instead of only $\mathbf{s}$. In the more physical context, we consider $\mathbf{F}(A, s)$ as our flux in the system and $\mathbf{a}$ as the geomorphic "response" to it. From the above empirical relation, we can see that the local growth $\partial h/\partial t$ is related simply to this flux $\mathbf{F}(A, s)$. Therefore, we expect that given some set of indexes (m, n), the local response $\mathbf{a}$ (which is a local transform of $h(\mathbf{x})$) should correlate with the flux calculated at the same local scale. This is because we assume that the empirical relation Eq. 5.4 should hold for quantities described at the same scale on the RHS and LHS. Furthermore, the general form of the relation may hold over a range of length scales with (m, n) dependent on the chosen observational scale.

We introduce the new quantity $\tilde{\mathbf{s}}_{mn}$ defined by

$$\tilde{\mathbf{s}}_{mn}(\mathbf{x};L_s)=\langle A^m s^n \hat{\mathbf{s}}\rangle_{L_s}=\frac{\int_{|\mathbf{x}'-\mathbf{x}|\leq L_s/2} d\mathbf{x}' g\left(\frac{\mathbf{x}'-\mathbf{x}}{L_s}\right) A^m|\nabla h(\mathbf{x}')|^n\hat{\mathbf{s}}}{\int_{|\mathbf{x}'-\mathbf{x}|\leq L_s/2} d\mathbf{x}' g\left(\frac{\mathbf{x}-\mathbf{x}'}{L_s}\right)} \tag{5.5}$$

where $g(\mathbf{x}-\mathbf{x}'/L_s)$ is the same as in Eq. 2.8. and concentrate our study on the correlation function

$$W=\frac{\langle|\mathbf{a}.\tilde{\mathbf{s}}_{mn}|^2\rangle}{\langle|\mathbf{a}|^2|\tilde{\mathbf{s}}_{mn}|^2\rangle}=\frac{\langle|\mathbf{a}|^2|\tilde{\mathbf{s}}_{mn}|^2\cos^2\delta\theta\rangle}{\langle|\mathbf{a}|^2|\tilde{\mathbf{s}}_{mn}|^2\rangle}. \tag{5.6}$$

which is the weighted average angular separation of $\mathbf{a}$ and $\tilde{\mathbf{s}}_{mn}$. Previous analysis shows that when $\mathbf{s}$ is computed at a particular scale L_s^* and $\mathbf{a}$ computed at a fixed ℓ_c, the correlation between the two becomes optimized and this happens at $L_s^* > \ell_c$. With the new flux function $\tilde{\mathbf{s}}_{mn}$, we expect the optimum scale L_s^* to become smaller and moves towards ℓ_c, ie. introducing A has the effect of collapsing the previous nonlocality to become more localized. We have made the conclusion based on the previous analysis that local anisotropy is correlated most with large scale structures (or slope). But A is a nonlocal, global function of $h(\mathbf{x})$, and so our $\tilde{\mathbf{s}}_{mn}$ has incorporated information about large scale structures in a local manner. Therefore, we have in a sense relocalized our flux to coincide with that of local anisotropy. Referring to Fig. 5-1, if we inquire about a set of A_i near the outlet of a basin, they would contain information about large scale topographic structures covering the basin that drains into that outlet.

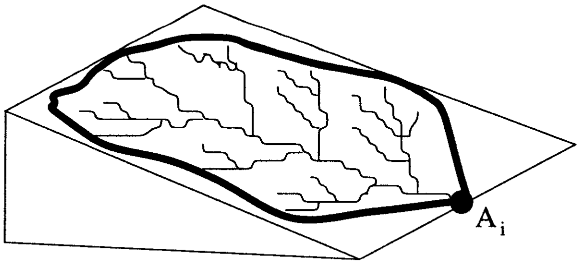

Figure 5-1: A_i is a global function in the sense that it depends on the structure of $h(\mathbf{x})$ within the basin. A set of A_i near the outlet therefore contain informations about the large scale topographical structures covering the basin that drains into it.

5.3 Results from empirical study

Fig. 5-2 shows W as function of L_s. Note that for each fixed ℓ_c, the length scale of optimal correlation L_s^* is being scaled back as function of increasing m. The magnitude of the correlation itself also improves as increasing m. For the series of plots, we are fixing $n = 1$. $n = 1$ seems to give the best correlation functions, this is supported with figures given in Fig. D-1, D-2, D-3, D-4 and D-5.

This shows that including the total contributing area A and making it more and more significant by raising it to a certain power, the correlation length L_s^* becomes more and more localized. This is expected based on the physical reasons given in the last section.

It is also elucidating to plot W as a function of L_s/ℓ_c and illustrate the relative extent of collapse of L_s^*, we pick the set with $\ell_c = 3.8$ km.

In each case, there is a unique m which depends on the value ℓ_c that gives $L_s^*/\ell_c \simeq 1$. At this m, the flux and the "response" coincide at the same scale. We show the case of $\ell_c = 5.7$ km in Fig. 5-5.

Although we show here only $\ell_c = 5.7$ km and demonstrate that when $m = 3$, $L_s^*/\ell_c \simeq 1$, the absolute value of L_s^* in km seems to be independent of ℓ_c. This is demonstrated in Fig. 5-6 where $m = 3$ and W is plotted against L_s.

Since we know that L_s^* does not depend very much on ℓ_c but mostly on m. We can just pick a particular ℓ_c, and concentrate on how W and L_s^* depend on m. For the case of $\ell_c = 3.8$ km, we present $W(L_s)$ for $m = 3$–10 in Fig. 5-7

Inspired by how $W(L_s)$ changes with m, it may be possible to rescale W and L_s by a power of m to have all the curves for different m collapse on top of each other. This is indeed the case when we attempt a scaling collapse of the curves. This is shown in Fig. 5-8.

It is observed that the curves collapse with deviation for large L_s due to finite size effect. We can write the scaling relation as:

$$W = m^{\beta} F\left(\frac{L_s}{m^{\alpha}}\right) G\left(\frac{L_s}{L_s^*}\right) \tag{5.7}$$

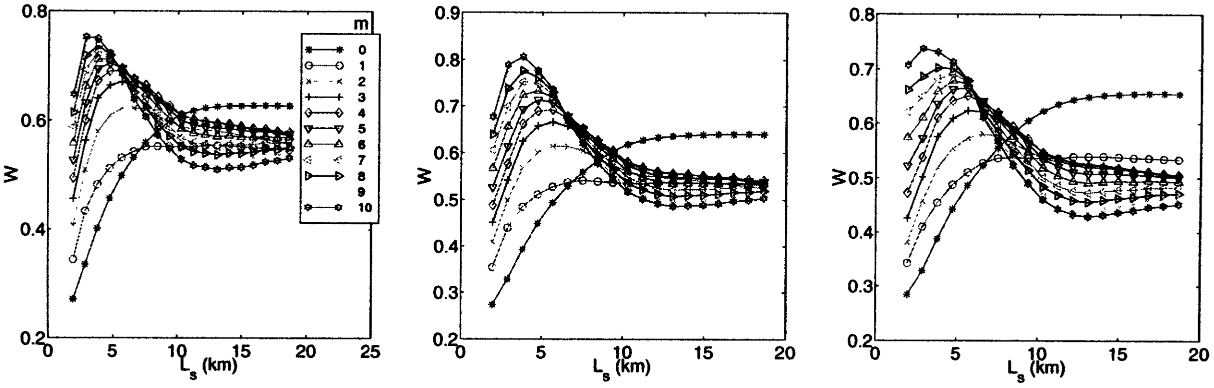

(a) $\ell_c = 2.88$ km

(b) $\ell_c = 3.80$ km

(c) $\ell_c = 4.73$ km

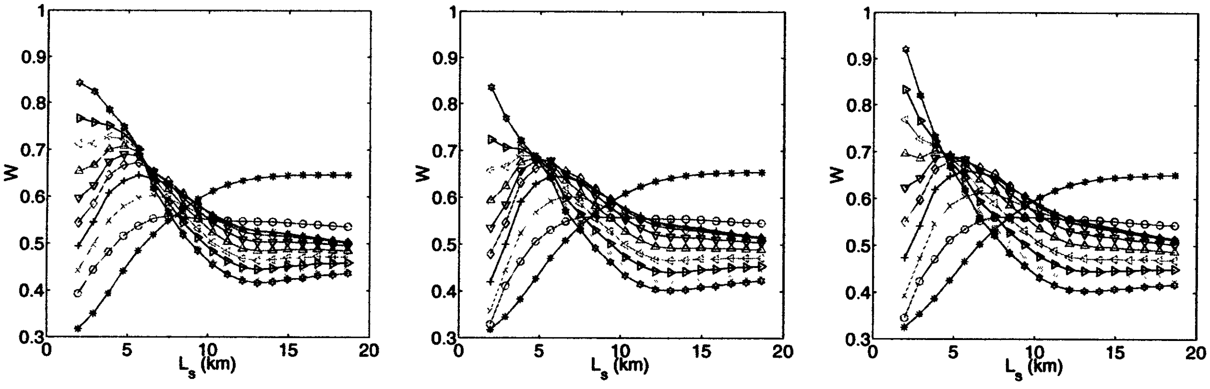

(d) $\ell_c = 5.66$ km

(e) $\ell_c = 6.59$ km

(f) $\ell_c = 7.51$ km

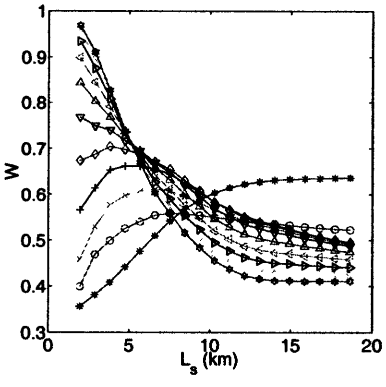

(g) $\ell_c = 8.44$ km

Figure 5-2: Results for 121°W/39°N to 120°W/38°N, $n = 1$ in all of the above.

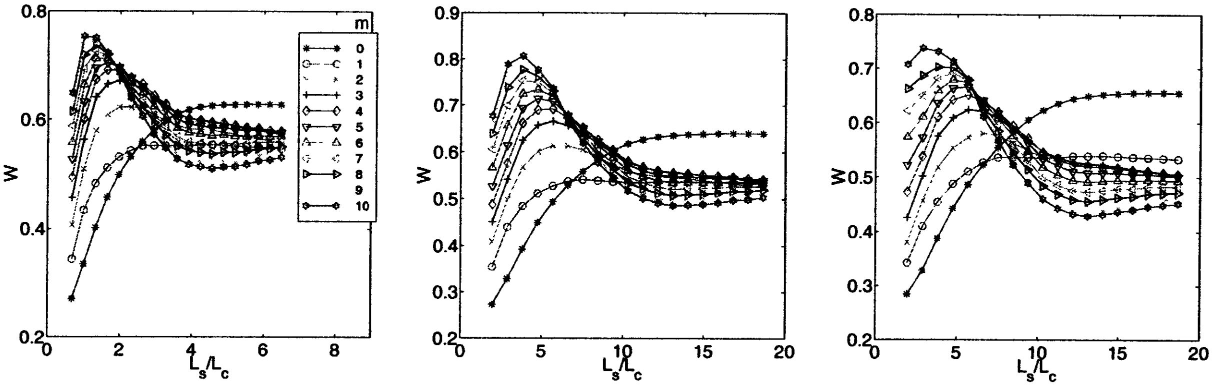

(a) $\ell_c = 2.88$ km (b) $\ell_c = 3.80$ km (c) $\ell_c = 4.73$ km

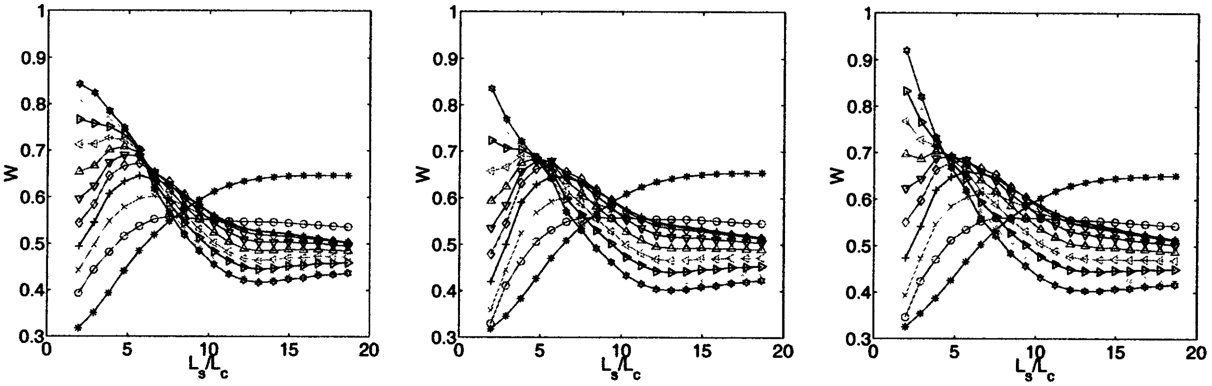

(d) $\ell_c = 5.66$ km (e) $\ell_c = 6.59$ km (f) $\ell_c = 7.51$ km

Figure 5-3: Results for 121°W/39°N to 120°W/38°N, $n = 1$ in all of the above (Part 1).

where $F(x)$ is a simple function that has a global maximum at a certain value x^* and $G(x)$ deviates from unity for large x which incorporates the finite size effect. For $\ell_c = 3.8$ km, α and β are measured respectively at -0.3 and 0.15. At x^*, we have $L_s^*/m^\alpha =$ constant and that

$$L_s^* \sim m^\alpha \tag{5.8}$$

If we locate L_s^* before the collapse and plot this against m, we obtain a test of the above relation. The result is shown in Fig. 5-9

We discover that $L_s^* \sim m^{-0.3}$.

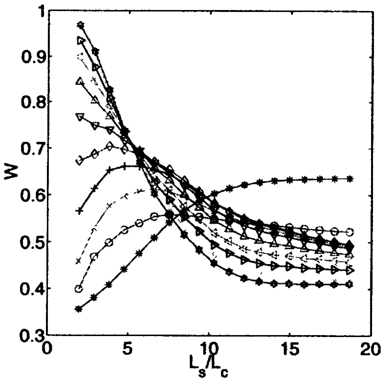

Figure 5-4: Results for 121°W/39°N to 120°W/38°N, $n = 1$ and $\ell_c = 8.44$ km (Part 2).

In summary, we have confirmed in another way that the flux is related to both the total contributing area (or discharge) and the local slope. Therefore, any theoretical models must hint at such a relation, ie. the local dynamics must somehow include information about A_i and the local slope $\mathbf{s} = \nabla h$.

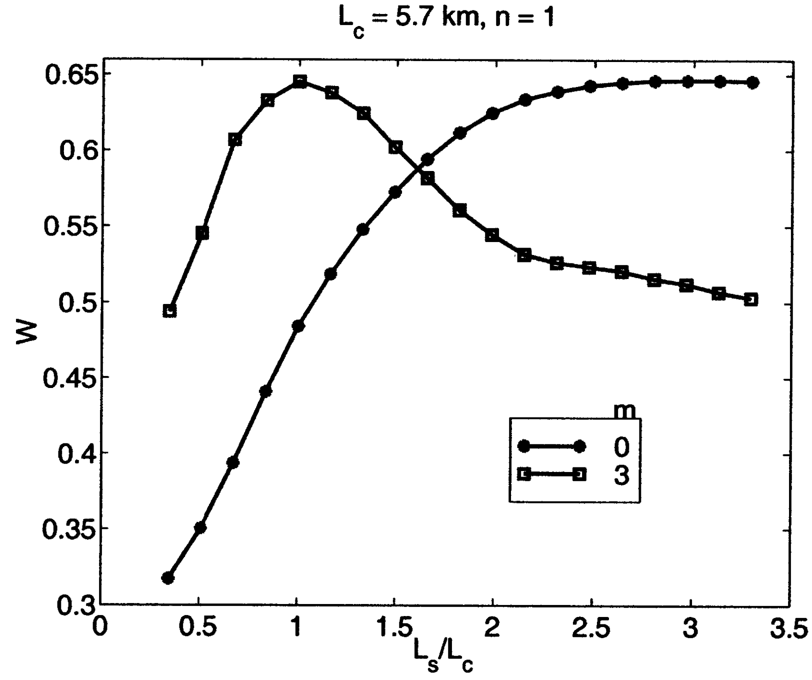

Figure 5-5: Showing that $L_s^*/\ell_c \simeq 1$ at $m = 3$ and $n = 1$

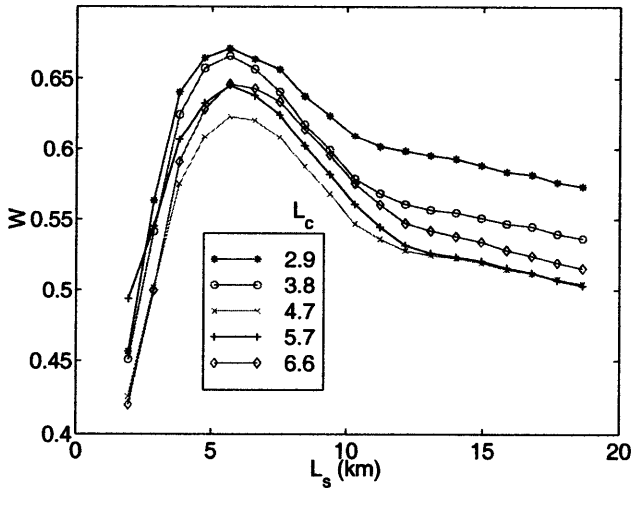

Figure 5-6: Showing that L_s^* does not depend very much on ℓ_c (shown for $m = 3$).

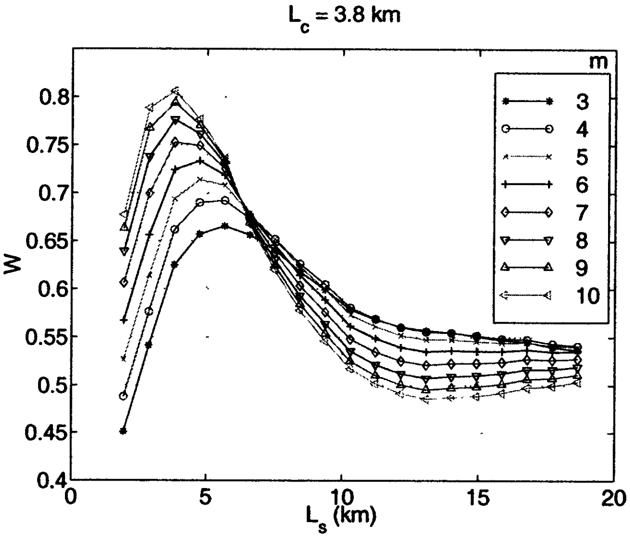

Figure 5-7: $W(L_s)$ depend on m

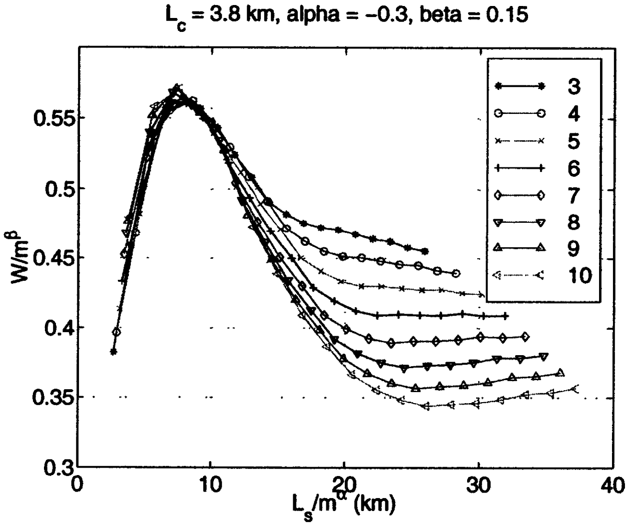

Figure 5-8: W and L_s can be rescaled by m^β and m^α to collapse on top of each other. The deviation at large L_s is finite size effect.

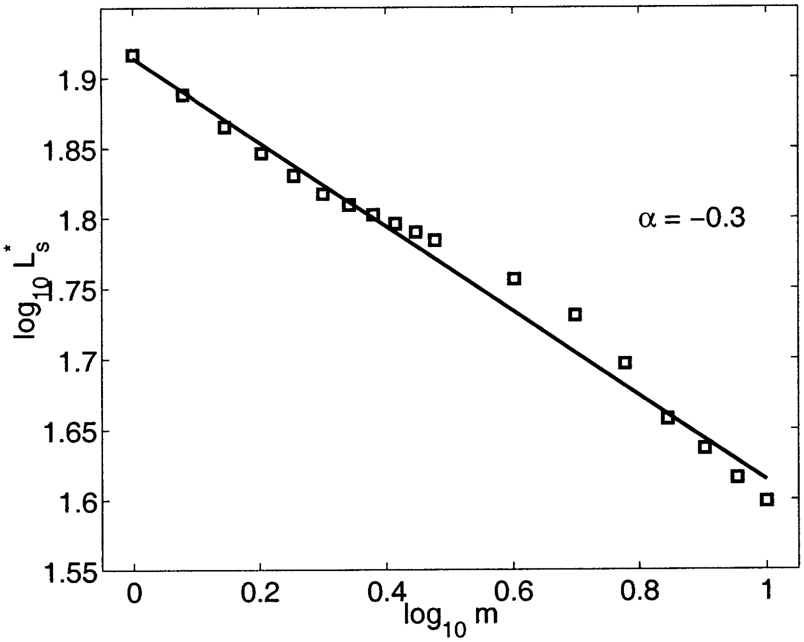

Figure 5-9: $L_s^* \sim m^{-0.3}$ for $\ell_c = 3.8$ km

Chapter 6

Conclusions

Anisotropic correlations appear to be a fundamental property of small scale erosion. In conclusion, we have demonstrated explicitly that anisotropy (channels) measured at small scales ℓ_c is coupled to topographic structures (drainage basins) measured at large scales L_s^*, $L_s^* \gg \ell_c$. This is counter-intuitive to the idea that anisotropy should be most correlated to the local slope ∇h measured at the same scale. This coupling across length scales suggests that processes (of surface erosion) at different scales interact, indicating one aspect of the nonlinear character of the underlying equations of surficial erosion. The use of local transformations have allowed us to systematically study this coupling of scales. The method is general enough to be applied to cases that do not show explicit self-affinity, (eg. no power law in the height-height correlation function). Empirically, we find that L_s^* depends on ℓ_c approximately as $L_s^* \sim \log \ell_c$. The optimal correlation length scale increases with increasing ℓ_c. Furthermore, L_s^* is related to the large scale topographical features of the landscape under study. We quantitatively demonstrate this fact by comparing the behaviors of L_s^* and the characteristic drainage basin size under different degrees of coarse-graining. The drainage basin size can be computed via total contributing area A and $L_s^* \simeq \langle A \rangle^{1/2}$. This indicates that the local anisotropy (channels and networks) at a point carries informations (long-range correlated) about large-scale topographic features up to a length scale roughly equals to the linear extent of the drainage basin (that drains through the point in question). This reveals quantitatively the nonlocal nature of surficial erosion.

Furthermore, regarding $\tilde{\mathbf{s}}_{mn}$ (defined as $\langle A^m s^n \hat{\mathbf{s}}\rangle_{L_s}$) as our generalized "stress" and $\mathbf{a}$ as a surrogate response, the localization of the correlations indicates that $\mathbf{a}$ is best characterized as a response to $\tilde{\mathbf{s}}_{mn}$ when both are defined at the same scale L. This is indeed confirmed in our empirical study. By increasing m, L_s^* moves closer to ℓ_c and may even get smaller with $L_s^* < \ell_c$. We discover a relation between L_s^* and m which is algebraic and independent (or weakly dependent) of ℓ_c. The power law relation is found to be $L_s^* \sim m^{-0.3}$. The explanation and origin of this power law relation is yet to be determined, and will be the subject of future investigations. We conclude that continuum models of erosion based on the postulate that sediment flux is proportional to $a^m s^n$ implicitly choose a scale when m and n are specified. While river networks exhibit many aspects of scale invariance [7], the landscapes that contain them nevertheless possess scale-dependent complexity [18] and characteristics. In our analysis, we implicitly regard landscapes as spatially extended pattern-forming (channels and networks) systems and how they correlate with the relief and basin structures while past studies have concentrated on some projections of these.

Tests on other landscapes indicate that the trends reported in this paper are not unusual. Conversely, tests on synthetic isotropic self-affine landscapes show neither coupling between channels and basins nor any systematic scale dependence and quantites. This strongly suggests that our quantitative analysis can "probe" beyond the self-affinity generalization and establishes natural landscapes pattern as a universal subclass with their own peculiar scale-dependent complexity distinct from other self-affine surfaces. Thus, our study (with possible further refinement) demonstrates one way in which landscape patterns of unknown origin [19] may be quantitatively analysed to determine the kind of mechanisms that have eroded them.

Appendix A

Wave packet

Consider the wave packet:

$$W_{\ell_c}(\mathbf{r}) = \frac{1}{\ell_c^2} \exp\left[\imath\mathbf{kr} - 8\left(\frac{r^2}{\ell_c^2}\right)\right] \tag{A.1}$$

$$C(\mathbf{r}, \phi;\, \ell_c) = \frac{1}{\ell_c^2} \left| \int_{|\mathbf{r}-\mathbf{r}'| \leq \ell_c/2} \mathrm{d}\mathbf{r}'\, W_{\ell_c}(\mathbf{r}' - \mathbf{r}, \phi)\ h(\mathbf{r}') \right| \tag{A.2}$$

With $\mathbf{r} = 0$ and $h(\mathbf{r}) = \exp(\imath\mathbf{k}'\mathbf{r})$ and exchanging $\mathbf{r}' \to \mathbf{r}$,

$$\begin{aligned}
C &= \frac{1}{\ell_c^2} \left| \int_{|\mathbf{r}| \leq \ell_c/2} \mathrm{d}\mathbf{r}\, W_{\ell_c}\left(\frac{\mathbf{r}}{\ell_c}, \phi\right)\ \exp(\imath\mathbf{k}'\mathbf{r}) \right| & \text{(A.3)} \\
&= \frac{1}{\ell_c^2} \left| \int_{|\mathbf{r}| \leq \ell_c/2} \mathrm{d}\mathbf{r}\ \exp\left[\imath(\mathbf{k}' - \mathbf{k})r\right] \exp\left[-\frac{8r^2}{\ell_c^2}\right] \right| & \text{(A.4)} \\
&= \frac{1}{\ell_c^2} \left| \int_{-\ell_c/2}^{\ell_c/2} \mathrm{d}x \exp\left[\imath(k_x' - k_x)x\right] \exp\left[-\frac{8x^2}{\ell_c^2}\right] \int_{-\ell_c/2}^{\ell_c/2} \mathrm{d}y \exp\left[\imath(k_y' - k_y)y\right] \exp\left[-\frac{8y^2}{\ell_c^2}\right] \right|
\end{aligned}$$

Extending the limit of integration to $+\infty$ and $-\infty$, we have

$$\begin{aligned}
C &= \exp\left[-\frac{(k_x' - k_x)\ell_c^2}{32}\right] \exp\left[-\frac{(k_y' - k_y)\ell_c^2}{32}\right] \frac{\pi}{8} \\
&= \exp\left[-\frac{\ell_c^2}{32}(\mathbf{k}' - \mathbf{k})^2\right] \frac{\pi}{8} & \text{(A.5)}
\end{aligned}$$

If $\mathbf{k}' = \mathbf{k}$, then $C \propto$ constant. But if $\mathbf{k}' \neq \mathbf{k}$, then $C \propto \exp[-\ell_c^2(\Delta\mathbf{k})^2]\ell_c^2$. Assuming on the average $\langle(\Delta\mathbf{k})^2\rangle \propto$ constant, then $C \propto \exp[-\ell_c^2]$.

This shows that our renormalization factor $1/\ell_c^2$ keeps C constant when $h(\mathbf{x})$ is a simple plane wave with $\mathbf{k}' = \mathbf{k}$. But in reality, even if $\mathbf{k}' = \mathbf{k}$, C is a function of ℓ_c for a certain range unless $\ell_c \gg \lambda$. This is partly due to the artefact of discretization. We also make the approximation of infinite limit of integration, where in actual implementation, we only integrate up to 2 standard deviations of the Gaussian and consider it as the cutoff. Finally, since the wave train is finite, its power spectrum is necessarily impure (ie. contains higher harmonics), and $\mathbf{k}' = \mathbf{k}$ is only approximately true.

All the above contributions become insignificant in the limit $\ell_c \gg \lambda \gg a$, where a is the lattice unit. We can test this quantitatively by preparing a plane wave with fixed wavelength (or $\mathbf{k}$), and measure the average magnitude of $\mathbf{a}$ (the director), $\langle|\mathbf{a}|\rangle$, where $\langle\rangle$ is taken to be averaging over space. See Fig. A-1

The figure shows that for $\ell_c/\lambda \geq 10$, $\mathbf{a}$ becomes properly normalized and independent of ℓ_c for a plane wave of fixed $\mathbf{k}' = \mathbf{k}$.

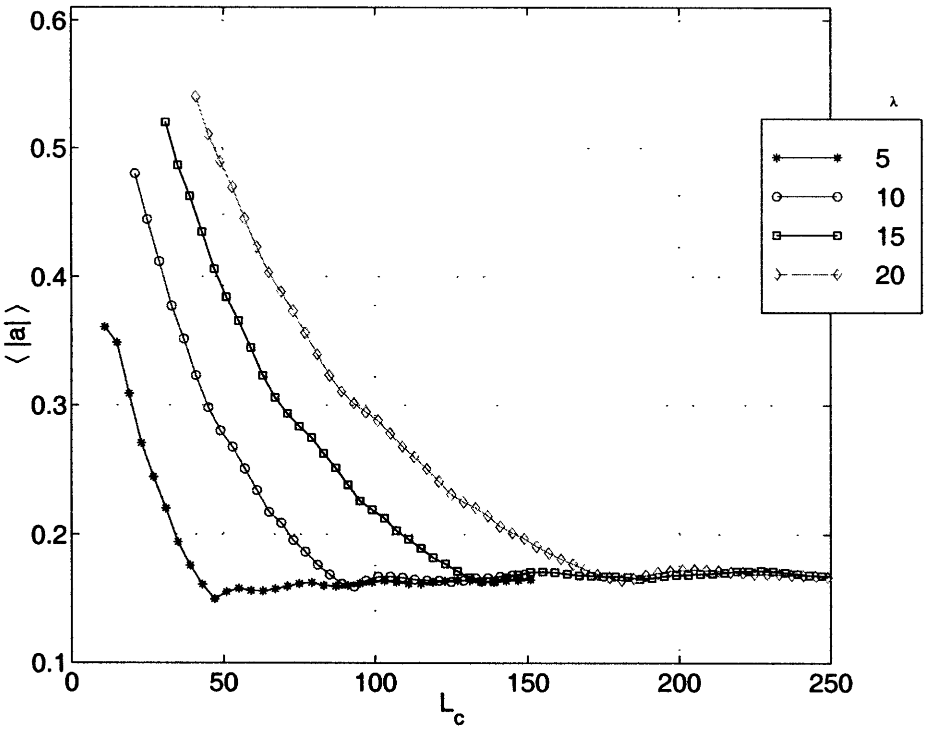

Figure A-1: Dependence of $\langle|\mathbf{a}|\rangle$ on ℓ_c with plane waves of different λ. It shows that for $\ell_c/\lambda \geq 10$, the effect due to discretization, finite cutoff integration, and finite size effect of plane wave becomes insignificant and $\langle|\mathbf{a}|\rangle$ becomes independent of ℓ_c for a fixed plane wave of $\mathbf{k}' = \mathbf{k}$.

Appendix B

Error Analysis

There are errors (besides errors from data resolutions and accuracies) that are related to projecting the earth's surface onto a two-dimensional plane. There are two main sources of interest:

1. The distance per unit grid spacing is actually a continuous function of the latitude. For example the distance between a unit grid spacing is larger at the equator than at a location near the poles.
2. The shortest distance between two points on a sphere is along the great circle rather than along the latitude (an error we commit in mapping the DEM data onto a planar rectangular grid.

By ignoring these two facts, we introduce a systematic error in the analysis, but we will show that these errors are relatively small for our purposes.

B.1 Error in assuming uniform grid

The most significant error of this sort comes from assuming that the length at top and bottom of the map are of the same length. For DEM given in 1 deg × 1 deg block. The perimeter at the top (near the pole) will have a shorter length than that of the bottom (near the equator). The largest error involved working with such DEM will be

$$|R_{\rm E}\delta\theta_{\rm long}(\cos\theta_{\rm top} - \cos\theta_{\rm bot})| \tag{B.1}$$

where $R_{\rm E}$ is the radius of the earth, $\delta\theta_{\rm long}$ is the longitudinal separation, and $\theta_{\rm top/bot}$ are the latitudes of the top and bottom perimeter.

For the piece of topography we studied, $R_{\rm E} = 6378136$ metres, $\delta\theta_{\rm long} = 1$ degree, $\theta_{\rm top} = 39^o$N, and $\theta_{\rm bot} = 38^o$N, which gives an error of about 1210 metres, or 13 grid units. (1 grid unit represents 92.764 metres). Comparing with the 1201 × 1201 grids we are working with, the error involved is just a little over 1% and can be neglected without affecting our statistical results.

B.2 Error in assuming the shortest distance between two points lies along the latitude

See Fig. B-1. Where

$$\begin{aligned} \delta\theta_{\rm long} &= \text{longitudinal separation.} \\ \theta_{\rm lat} &= \text{latitude.} \\ R_{\rm E} &= \text{radius of the earth.} \end{aligned}$$

1. Compute $\overline{\rm AB}$ (Fig. B-2): $\overline{\rm AD} = \overline{\rm DB} = R_{\rm E}\cos\theta_{\rm lat}$ Therefore,

$$\overline{\rm AB} = 2R_{\rm E}\cos\theta_{\rm lat}\sin\frac{\delta\theta_{\rm long}}{2} \tag{B.2}$$

2. Compute ∠ACB (Fig. B-3):

$$\Delta = 2\sin^{-1}\left[\frac{R_{\rm E}\cos\theta_{\rm lat}\sin\frac{\delta\theta_{\rm long}}{2}}{R_{\rm E}}\right] \tag{B.3}$$

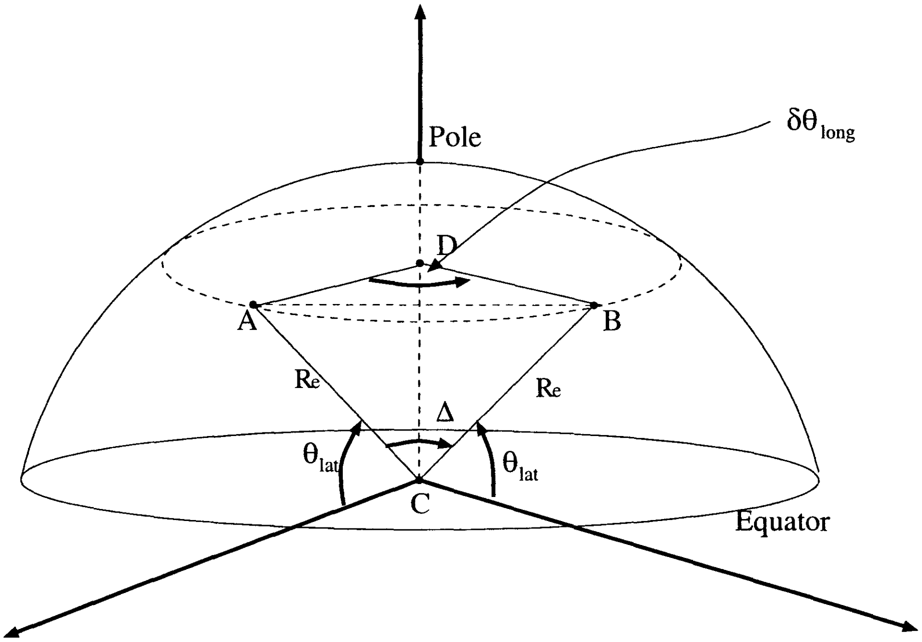

Figure B-1:

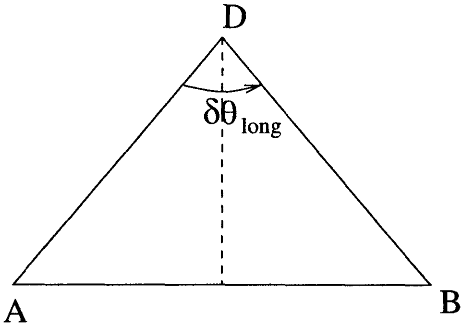

Figure B-2:

3. Finally, compute $\overline{\mathrm{AB}}$ along the great circle:

$$\text{length } \overline{\mathrm{AB}} \text{ along great circle} = 2\pi R_{\mathrm{E}} \frac{\Delta}{2\pi} = 2R_{\mathrm{E}} \sin^{-1}\left(\cos\theta_{\mathrm{lat}} \sin\frac{\delta\theta_{\mathrm{long}}}{2}\right) \tag{B.4}$$

Therefore, the absolute error resulting from taking this as the distance along

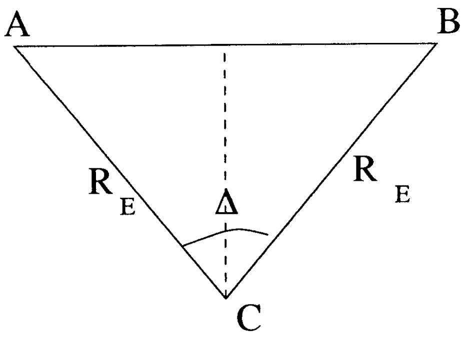

Figure B-3:

the latitude is:

$$\delta = \left| 2R_{\mathrm{E}} \sin^{-1}\left(\cos\theta_{\mathrm{lat}} \sin\frac{\delta\theta_{\mathrm{long}}}{2}\right) - R_{\mathrm{E}}\delta\theta_{\mathrm{long}} \cos\theta_{\mathrm{lat}} \right| \tag{B.5}$$

For the topography we are working with, this error comes out to be about 0.42 metres, or 0.005 grid unit. An error that is negligible.

Appendix C

Measuring Local Anisotropy of Plane Waves and Band Pattern

We apply our method of local transforms to extract the local anisotropic director field of a set of plane waves. This is just to convince ourselves that the proposed transforms can indeed correctly measure the local wave number **k**. The results are shown in Fig. C-2. Fig. C-1 shows the anisotropic director field for a pattern of stripes and bands.

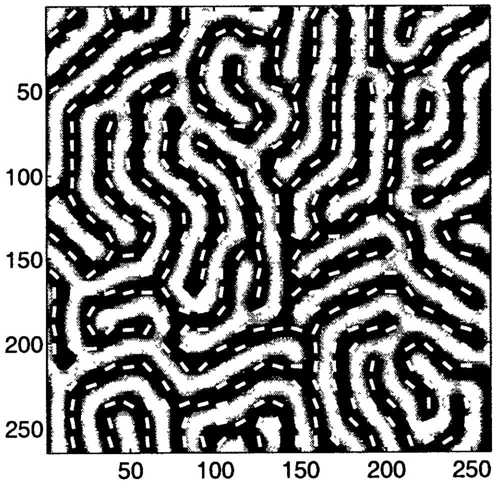

Figure C-1: Anisotropic director field for a pattern of stripes and bands.

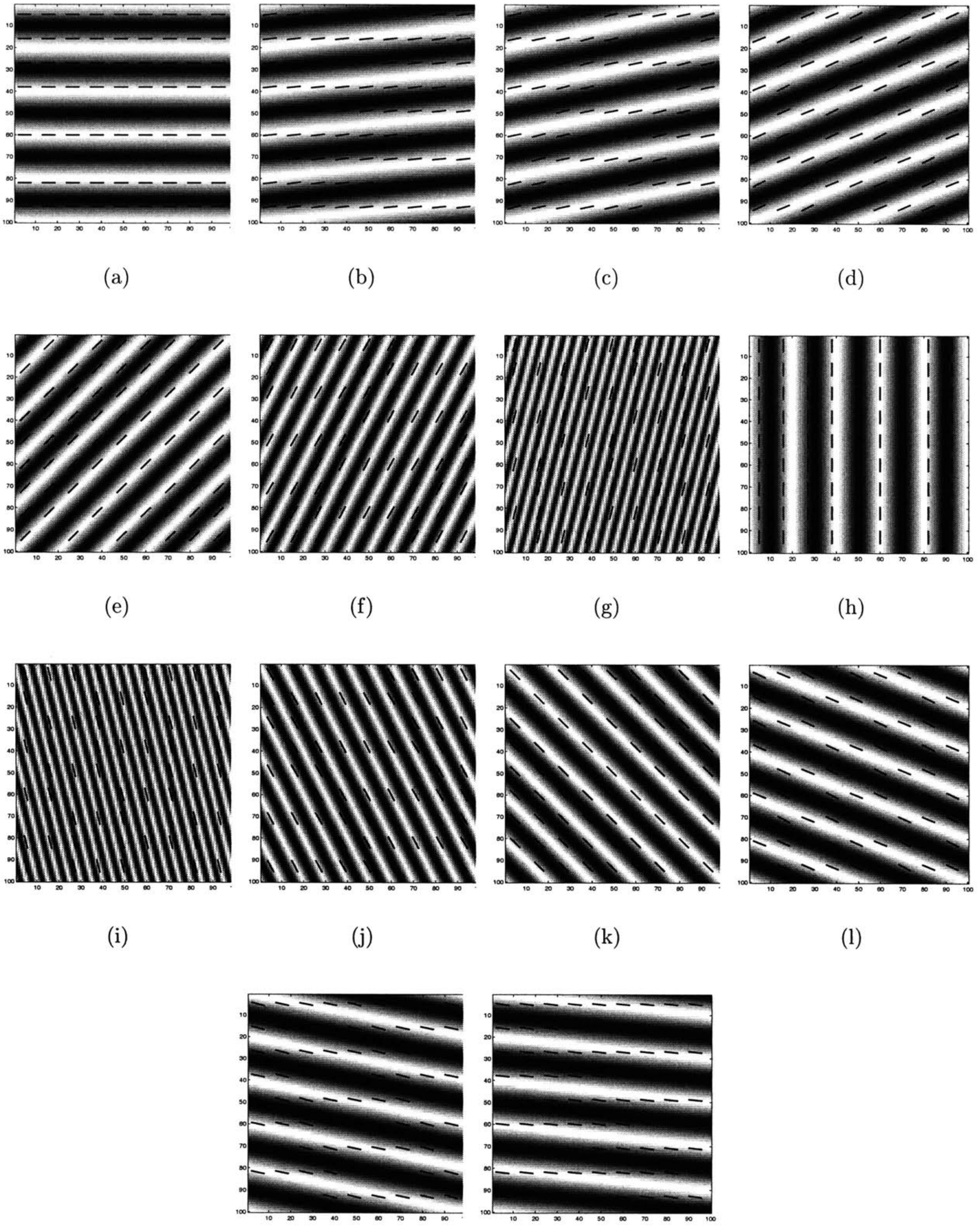

Figure C-2: Figures showing the local anisotropic director field for a set of plane waves

Appendix D

Data Exposition

Fig. D-1 shows plot of W vs L_s for different n and ℓ_c keeping $m = 0$.

Fig. D-2 shows plot of W vs L_s for different n and ℓ_c keeping $m = 1$.

Fig. D-3 shows plot of W vs L_s for different n and ℓ_c keeping $m = 2$.

Fig. D-4 shows plot of W vs L_s for different n and ℓ_c keeping $m = 3$.

Fig. D-5 shows plot of W vs L_s for different n and ℓ_c keeping $m = 4$.

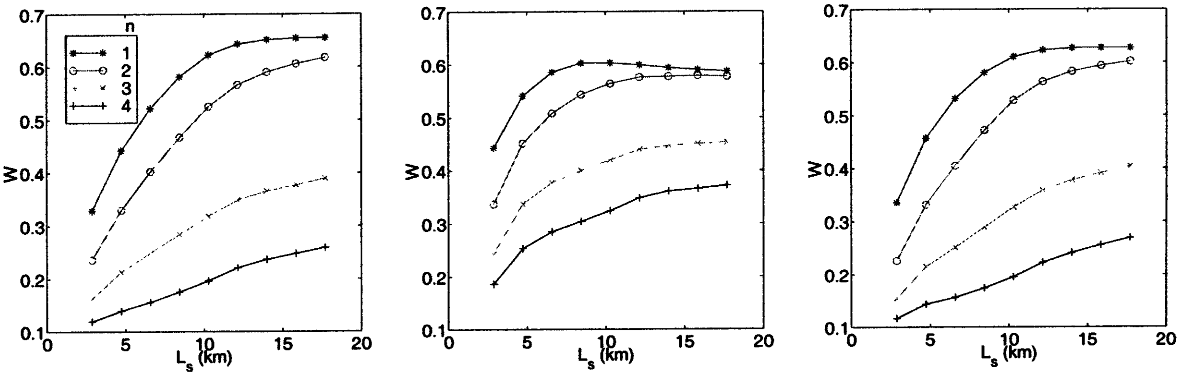

(a) $\ell_c = 1.02$ km

(b) $\ell_c = 1.95$ km

(c) $\ell_c = 2.88$ km

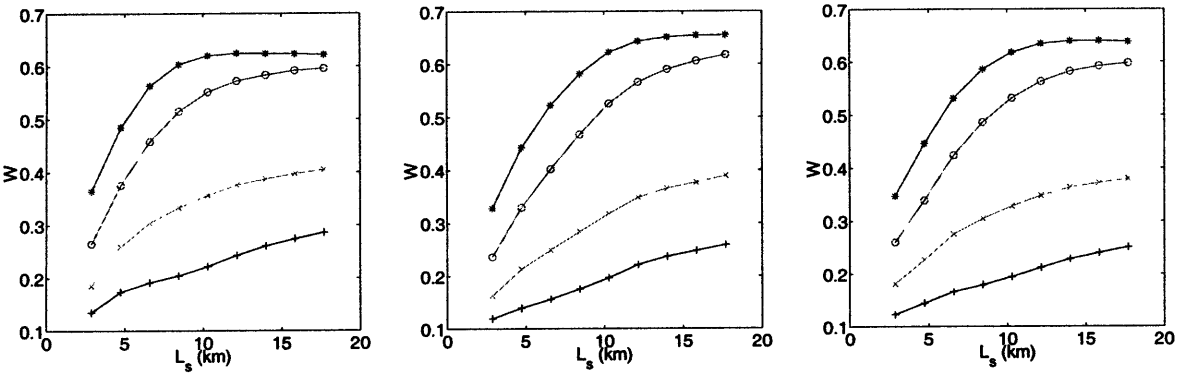

(d) $\ell_c = 3.80$ km

(e) $\ell_c = 4.73$ km

(f) $\ell_c = 5.66$ km

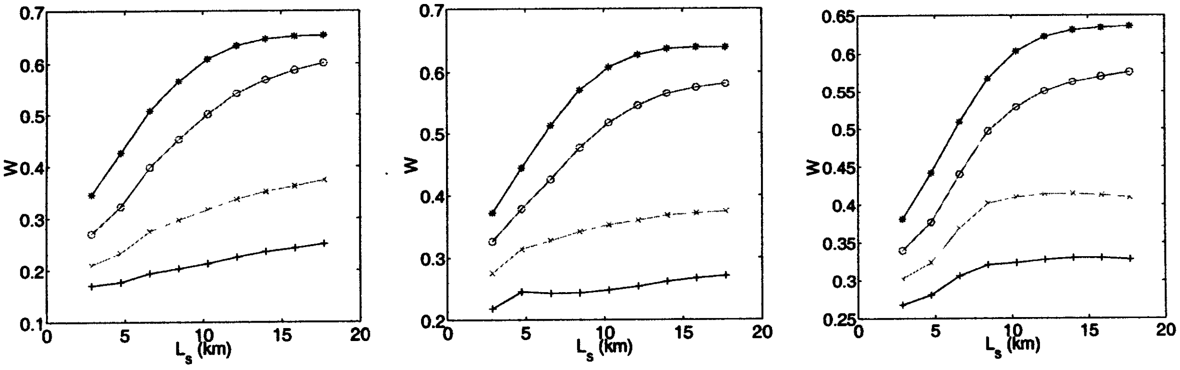

(g) $\ell_c = 6.59$ km

(h) $\ell_c = 7.51$ km

(i) $\ell_c = 8.44$ km

Figure D-1: Results for 121°W/39°N to 120°W/38°N, $m = 0$

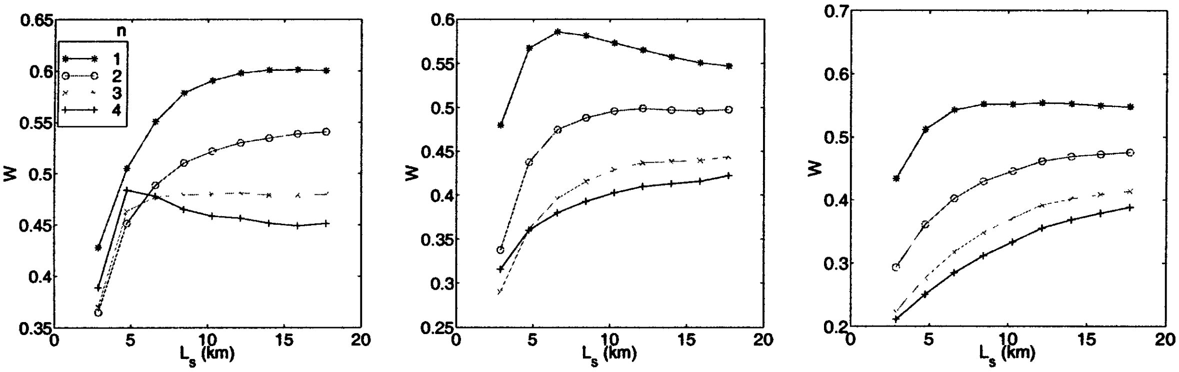

(a) $\ell_c = 1.02$ km

(b) $\ell_c = 1.95$ km

(c) $\ell_c = 2.88$ km

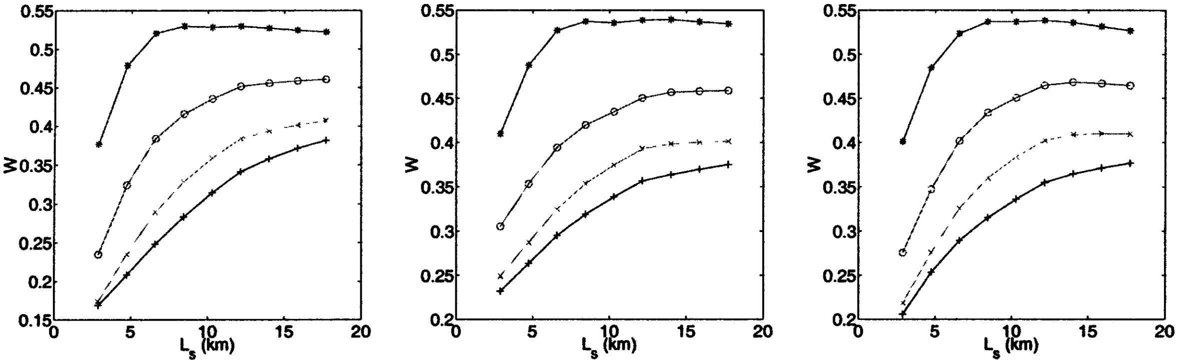

(d) $\ell_c = 3.80$ km

(e) $\ell_c = 4.73$ km

(f) $\ell_c = 5.66$ km

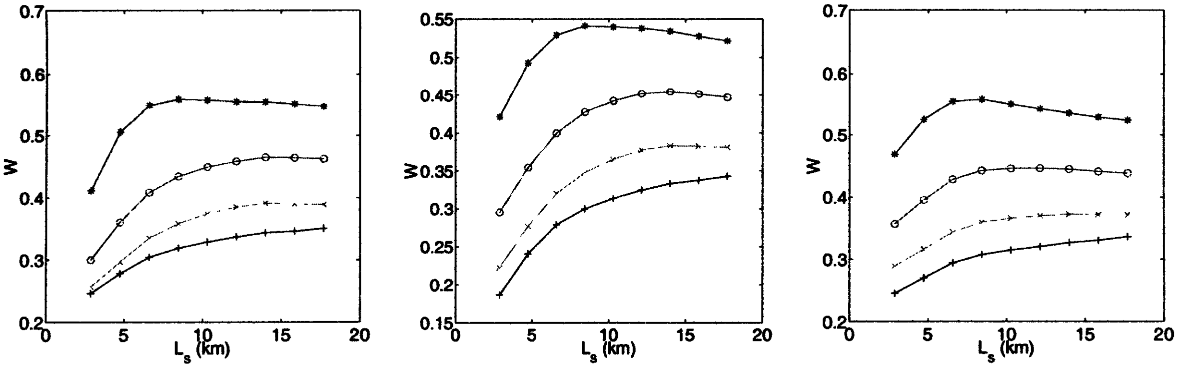

(g) $\ell_c = 6.59$ km

(h) $\ell_c = 7.51$ km

(i) $\ell_c = 8.44$ km

Figure D-2: Results for 121°W/39°N to 120°W/38°N, $m = 1$

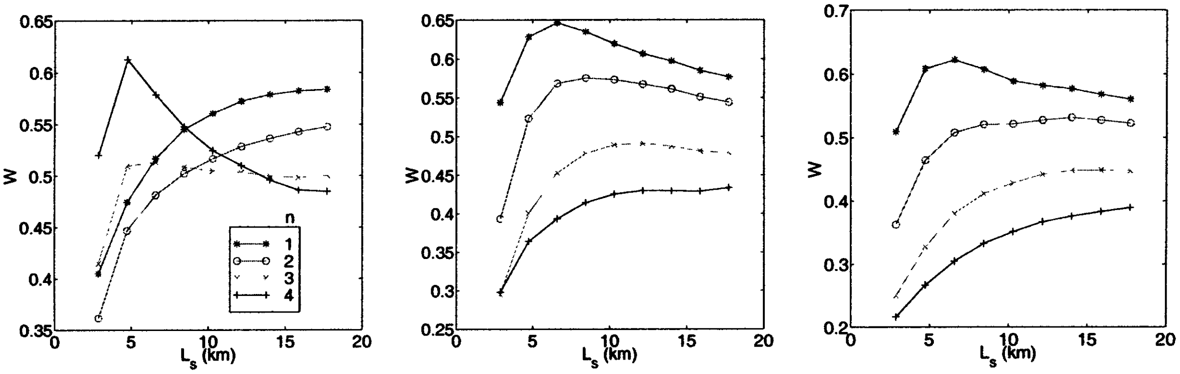

(a) $\ell_c = 1.02$ km (b) $\ell_c = 1.95$ km (c) $\ell_c = 2.88$ km

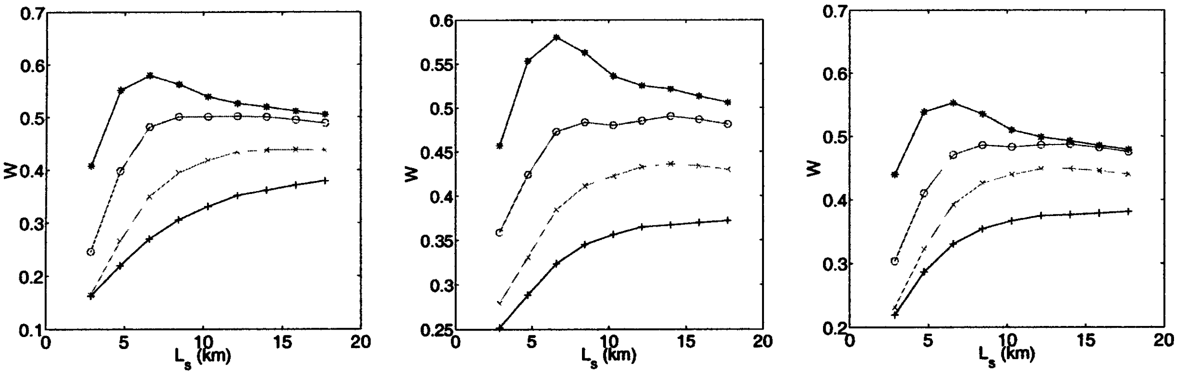

(d) $\ell_c = 3.80$ km (e) $\ell_c = 4.73$ km (f) $\ell_c = 5.66$ km

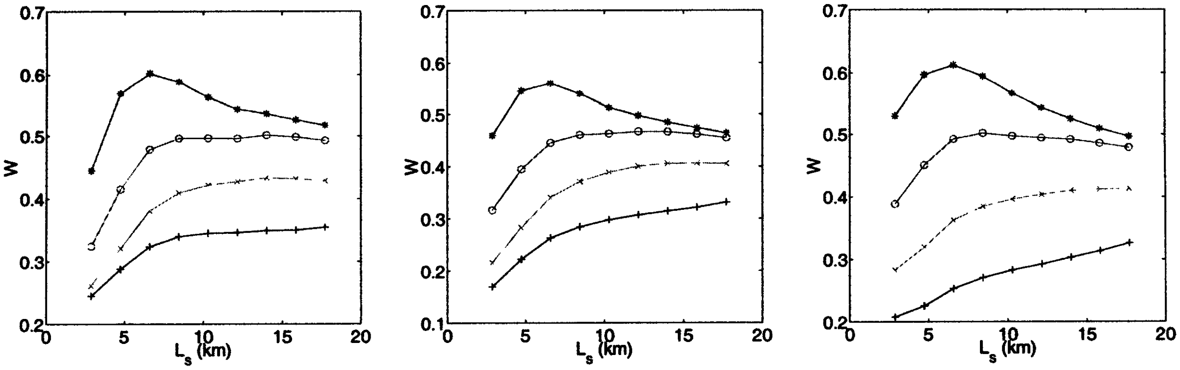

(g) $\ell_c = 6.59$ km (h) $\ell_c = 7.51$ km (i) $\ell_c = 8.44$ km

Figure D-3: Results for 121°W/39°N to 120°W/38°N, $m = 2$

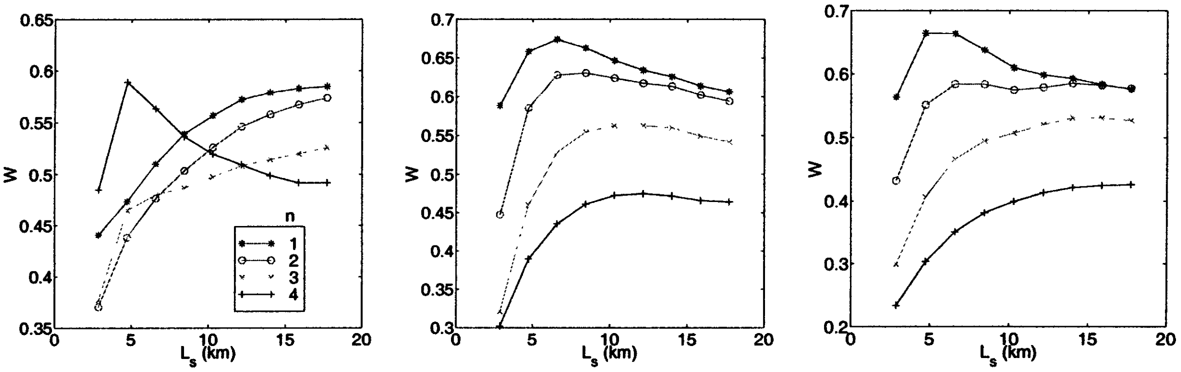

(a) $\ell_c = 1.02$ km

(b) $\ell_c = 1.95$ km

(c) $\ell_c = 2.88$ km

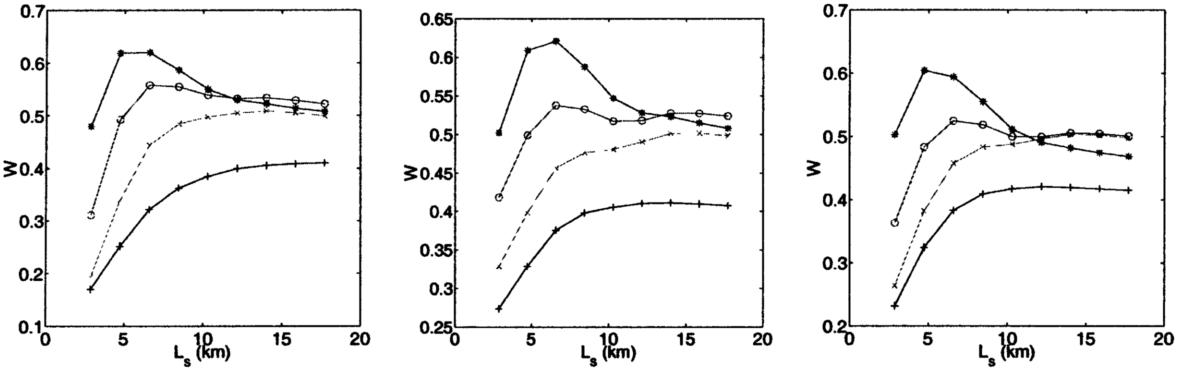

(d) $\ell_c = 3.80$ km

(e) $\ell_c = 4.73$ km

(f) $\ell_c = 5.66$ km

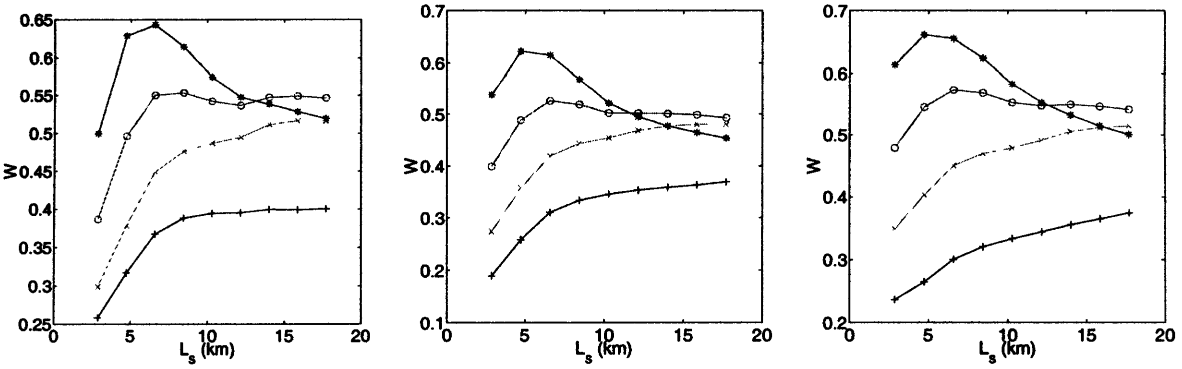

(g) $\ell_c = 6.59$ km

(h) $\ell_c = 7.51$ km

(i) $\ell_c = 8.44$ km

Figure D-4: Results for 121°W/39°N to 120°W/38°N, $m = 3$

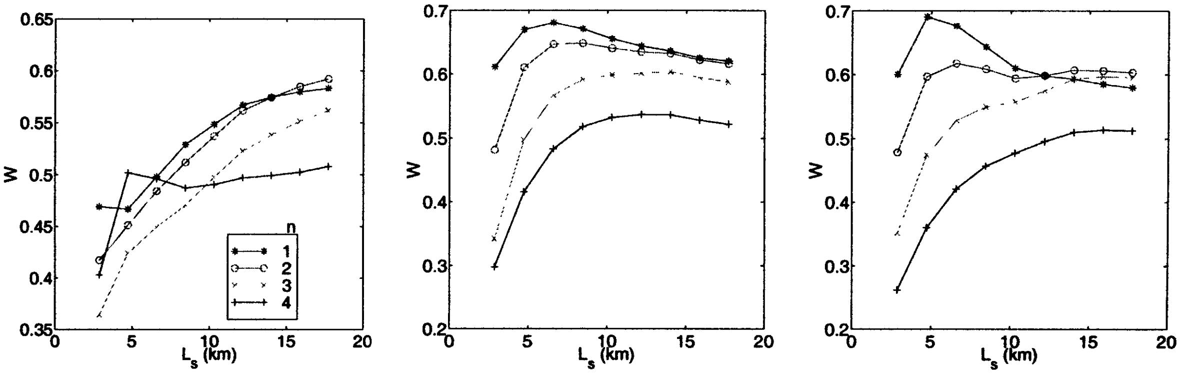

(a) $\ell_c = 1.02$ km (b) $\ell_c = 1.95$ km (c) $\ell_c = 2.88$ km

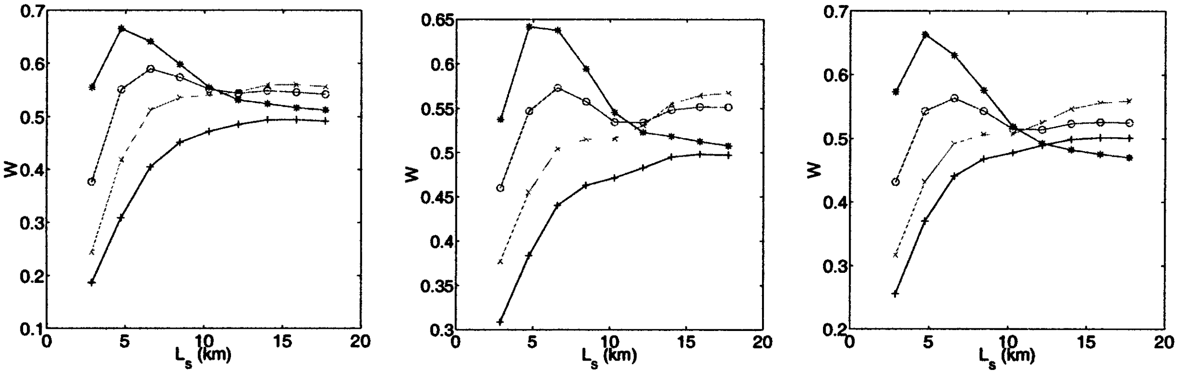

(d) $\ell_c = 3.80$ km (e) $\ell_c = 4.73$ km (f) $\ell_c = 5.66$ km

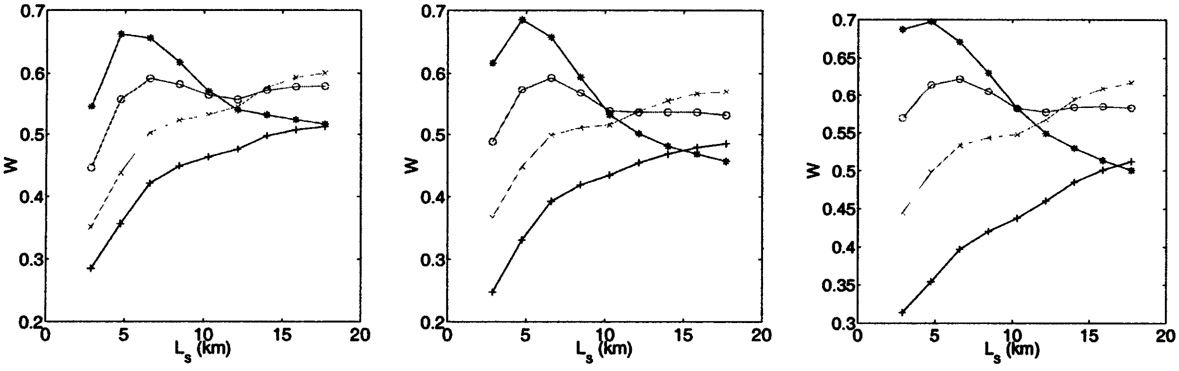

(g) $\ell_c = 6.59$ km (h) $\ell_c = 7.51$ km (i) $\ell_c = 8.44$ km

Figure D-5: Results for 121°W/39°N to 120°W/38°N, $m = 4$

Appendix E

Fractures

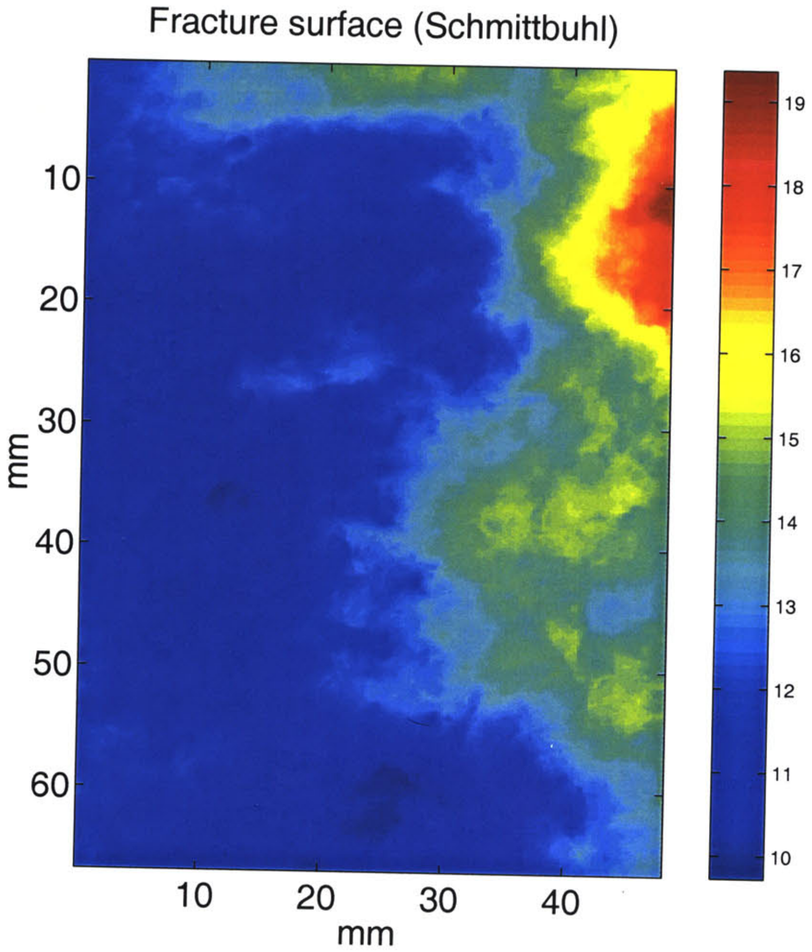

Figure E-1: ⟶ direction of crack propagation

Fig. E-1 shows topography of a fracture in a granite sample (after López and

Schmittbuhl [15]). The fracture was made by making a straight notch on one side of the granite sample and pulling the sample apart in the vertical direction with the direction of crack propagation perpendicular to it. We use the same method in analyzing landscape topography to the fracture topography. We can see in Fig. E-2 that the inclusion of the A^m field also relocalizes L_s^*. See Fig. E-3 also.

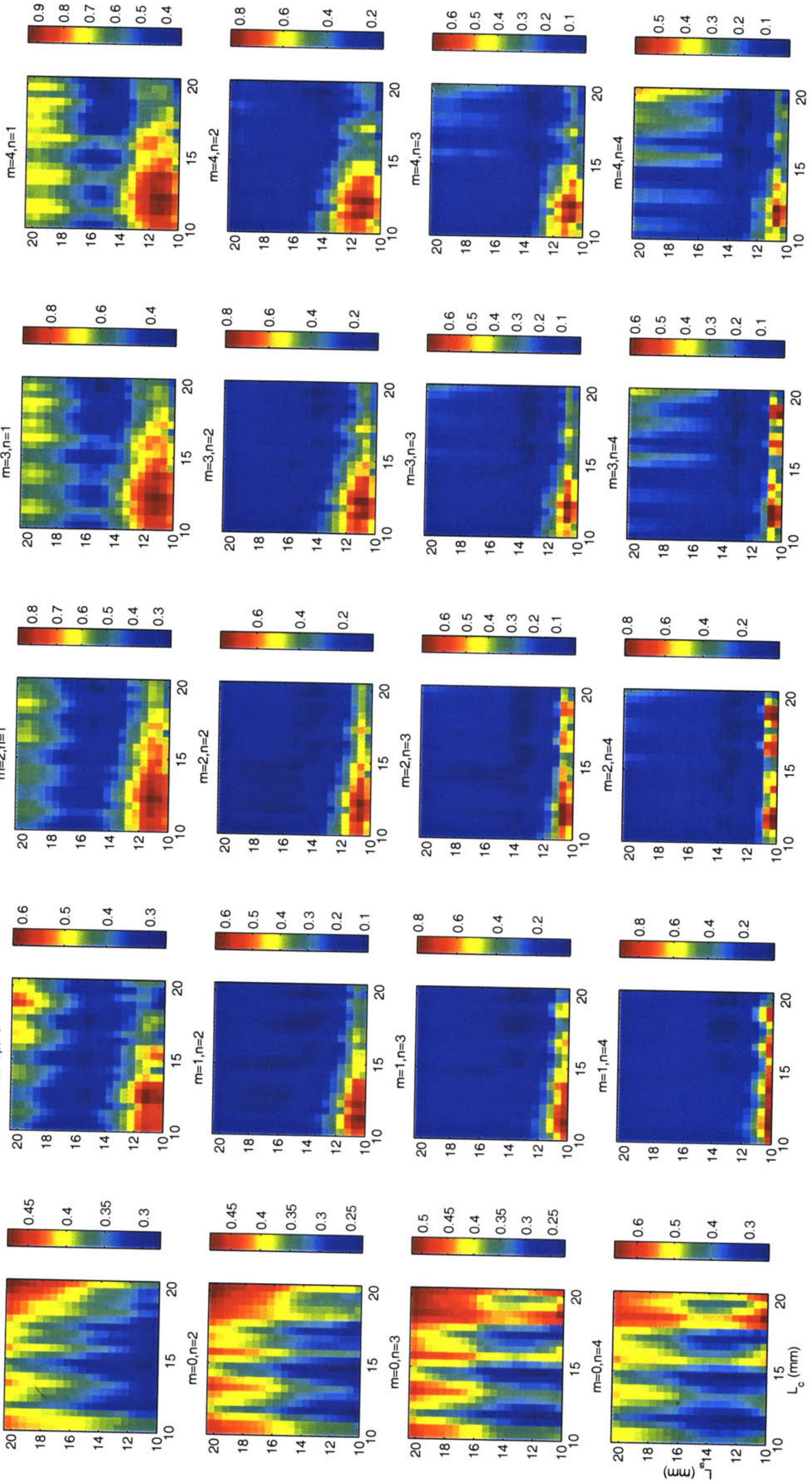

Figure E-2: Plots of W as a function of L_s and ℓ_c for different sets of m and n.

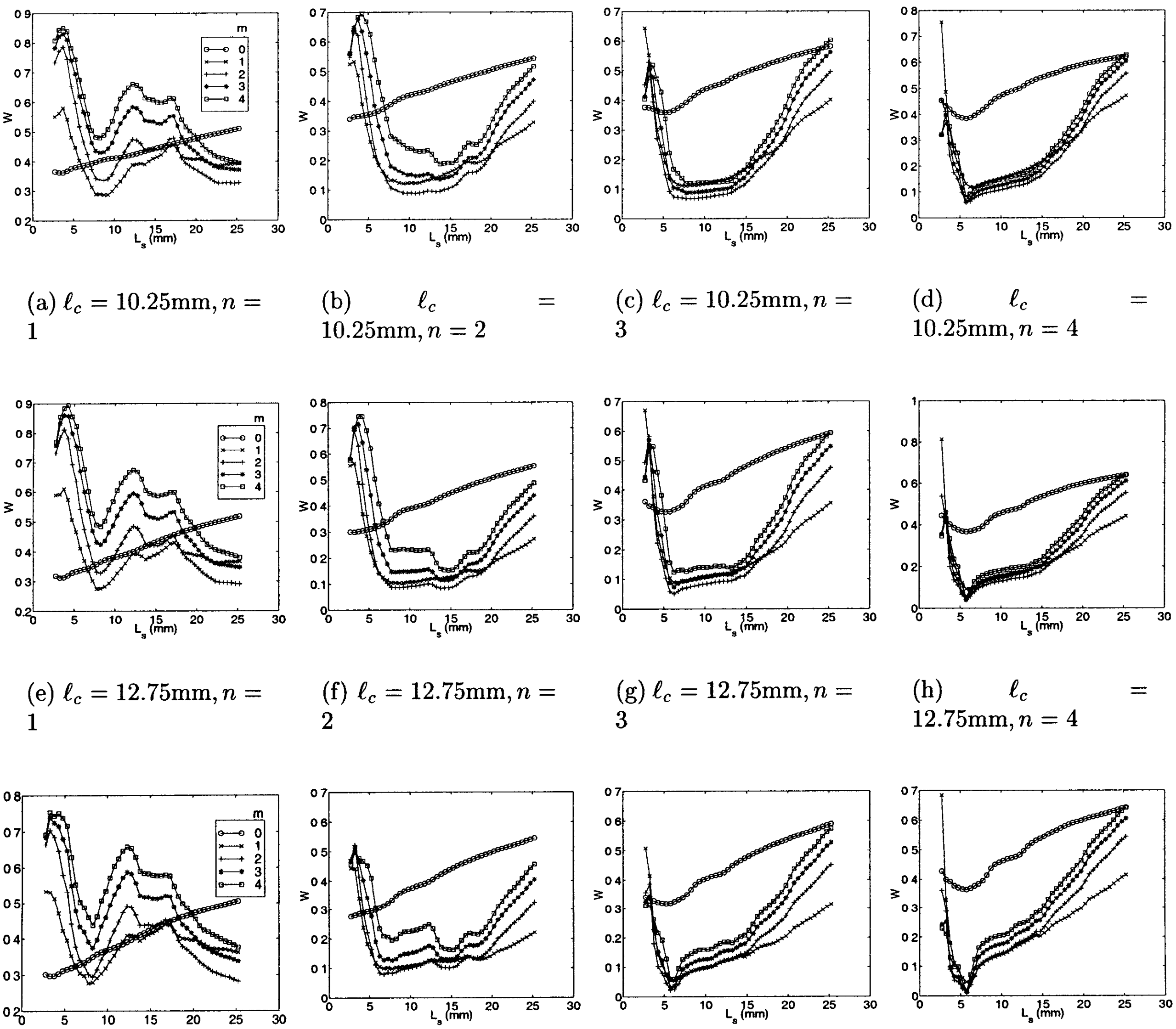

(a) $\ell_c = 10.25\text{mm}, n = 1$ (b) $\ell_c = 10.25\text{mm}, n = 2$ (c) $\ell_c = 10.25\text{mm}, n = 3$ (d) $\ell_c = 10.25\text{mm}, n = 4$

(e) $\ell_c = 12.75\text{mm}, n = 1$ (f) $\ell_c = 12.75\text{mm}, n = 2$ (g) $\ell_c = 12.75\text{mm}, n = 3$ (h) $\ell_c = 12.75\text{mm}, n = 4$

(i) $\ell_c = 15.25\text{mm}, n = 1$ (j) $\ell_c = 15.25\text{mm}, n = 2$ (k) $\ell_c = 15.25\text{mm}, n = 3$ (l) $\ell_c = 15.25\text{mm}, n = 4$

Figure E-3: Results for fracture topography

Bibliography

[1] B. B. MANDELBROT, *The Fractal Geometry of Nature* (Freeman, San Francisco, 19 82).

[2] A. E. SCHEIDEGGER, *Theoretical Geomorphology (3rd edition)*, (Springer-Verlag).

[3] W. I. NEWMAN AND D. L. TURCOTTE, Geophys. J. Int. **100**, 433 (1990)

[4] D. L. TURCOTTE, *Fractals and Chaos in Geology and Geophysics* (Cambridge University Press, New York, 1992).

[5] A. L. BARABASI AND H. E. STANLEY, *Fractal Concepts in Surface Growth*, (Cambridge University Press, 1995).

[6] R. PASTOR-SATORRAS AND D. H. ROTHMAN, *Stochastic Equation for the Erosion of Inclined Topography* Phys. Rev. Lett. Vol. **80**, pp. 4349–4352 (1998)

[7] I. RODRIGUEZ-ITURBE AND A. RINALDO, *Fractal River Basins: Chance and Self-Organization* (Cambridge University Press, Cambridge, England, 1997).

[8] KEVIN SINCLAIR AND ROBIN C. BALL, Phys. Rev. Lett. Vol. **76**(18), pp. 3360–3363 (1996).

[9] C. BOWMAN AND A. C. NEWELL, *Natural patterns and wavelets*, Rev. Mod. Phys. Vol.**70**, No. 1, pp. 289–301 (January 1998)

[10] D. A. EGOLF, I. V. MELNIKOV, AND E. BODENSCHATZ, Phys. Rev. Lett. **80**, 3228 (1998).

[11] P. Ball, *The self-made tapestry* (Oxford University Press, Oxford, 1999).

[12] D. L. Turcotte, *Fractals and Chaos in Geology and Geophysics* (Cambridge University Press, New York, 1992). p173

[13] Armanini, A., and G. Di Silvio, editors. 1992. *Hydraulics of Mountain Regions*, Springer-Verlag, Berlin.

[14] Rodriguez-Iturbe, I. et. al., *Power-law distributions of mass end energy in river basins.*, Water Resour. Res., **28**(4), 988–993.

[15] Juan M. López and Jean Schmittbuhl, Phys. Rev. E **57**, 6405 (1998)

[16] A. E. Scheidegger, Bull. Int. Assoc. Sci. Hydrol. 12 (1967) 15.

[17] K. Chan and D. H. Rothman (submitted to Nature).

[18] W. E. Dietrich and D. R. Montgomery, in *Scale Dependence and Scale Invariance in Hydrology*, edited by G. Sposito (Cambridge University Press, Cambridge, United Kingdom, 1998), pp. 30–60.

[19] M. H. Carr, *Water on Mars* (Oxford University Press, Oxford, 1992)